The Cryosphere Discuss., doi:10.5194/tc-2016-13, 2016
Manuscript under review for journal The Cryosphere
Published: 22 February 2016


# Sea Ice Deformation in a Coupled Ocean-Sea Ice Model and in Satellite Remote Sensing Data

Gunnar Spreen[1,2], Ron Kwok[1], Dimitris Menemenlis[1], and An T. Nguyen[1,3]

[1]Jet Propulsion Laboratory, California Institute of Technology, Pasadena, CA, USA.
[2]University of Bremen, Institute of Environmental Physics, Bremen, Germany.
[3]now at Massachusetts Institute of Technology, Cambridge, MA, USA.

*Correspondence to:* Gunnar Spreen (gunnar.spreen@uni-bremen.de)

**Abstract.** A realistic representation of sea ice deformation in models is important for accurate simulation of the sea ice mass balance. In this study, model ice strength sensitivity experiments show an increase in Arctic Basin sea ice volume of 7% and 35% for a decrease in ice strength of, respectively, 30% and 70%, after 8 years of model integration. This volume increase is caused by a combination of dynamic and thermodynamic processes. On the one hand, a weaker ice cover initially produces more ice due to increased deformation and new ice growth. The thickening of the ice, on the other hand, increases the ice strength and decreases the sea ice volume export out of the Arctic Basin. The balance of these processes leads to a new equilibrium Arctic Basin ice volume. Simulated sea ice deformation strain rates from model simulations with 4.5, 9, and 18-km horizontal grid spacing are compared with synthetic aperture radar satellite observations (RGPS). All three model simulations can reproduce the large-scale ice deformation patterns but they do not reproduce all aspects of the observed deformation rates. The overall sea ice deformation rate is about 50% lower in all model solutions than in the satellite observations, especially in the seasonal sea ice zone. Small scale sea ice deformation and linear kinematic features are not adequately reproduced. A decrease in model grid spacing, however, produces a higher density and more localized ice deformation features. Overall, the 4.5-km simulation produces the lowest misfits in divergence, vorticity, and shear when compared with RGPS data. Not addressed in this study is whether the differences between simulated and observed deformation rates are an intrinsic limitation of the viscous-plastic sea ice rheology that was used in the sensitivity experiments, or whether it indicates a lack of adjustment of existing model parameters to better represent these processes. Either way, this study provides new quantitative metrics for existing and new sea ice rheologies to strive for.

## 1 Introduction

The Arctic sea ice in many respects is an important component of the Earth's climate system, e.g., sea ice governs the ocean to atmosphere heat flux, freezing and melting influences the upper ocean salinity and density, and sea ice dynamics act as a latent energy transport (Barry et al., 1993). During recent years substantial changes of the Arctic sea ice cover have been observed (e.g., Comiso et al., 2008; Kwok and Rothrock, 2009; Nghiem et al., 2007). Coupled ocean-sea ice models can reproduce some aspects of sea ice and its recent changes (e.g., Zhang et al., 2008; Lindsay et al., 2009; Nguyen et al., 2011). In part this can be attributed to the fact that model parameters can be adjusted to produce observed ice concentration (extent) and drift distributions (Nguyen et al., 2011; Fenty et al., 2015). Detailed comparisons between satellite remote sensing data with model results, however, reveal big differences in certain aspects of the sea ice cover, e.g., for fracture zones and for small scale dynamic processes (Kwok et al., 2008; Girard et al., 2009). It remains unclear whether current model physics are suited to reproduce these observed sea ice deformation features (Coon et al., 2007) or if new sea ice rheologies like the one presented in Girard et al. (2011) have to be used. Sea ice deformation is an important process for (1) sea ice mass balance due to new ice production and ridged ice formation, (2) brine rejection into the ocean, (3) regulation of ocean-to-air heat and gas fluxes, and (4) altering the air and water drag coefficients. Therefore a realistic representation of sea ice deformation in coupled sea ice-ocean models is important.

Here we study sea ice deformation strain rates in the Arctic obtained from Synthetic Aperture Radar (SAR) satellite measurements using the RADARSAT Geophysical Processor System (RGPS) in comparison to coupled ocean-sea ice simulations carried out with the Massachusetts Institute of Technology general circulation model (MITgcm) as configured for the Estimating the Circulation and Climate of the Ocean, Phase II (ECCO2) project (Menemenlis et al., 2008). Model integrations with horizontal grid spacing of 18, 9, and $4.5$ km were carried out. As a baseline, the model sensitivity to the model ice strength parameterization is assessed. Thereafter the model solutions are compared both spatially and temporally to the satellite RGPS observations. These comparisons are used to address model uncertainties regarding sea ice deformation representation.

Traditionally sea ice model performance is evaluated by comparing satellite-derived ice area and velocities to model results (e.g., Nguyen et al., 2011; Zhang et al., 2003). However, it can be shown that the Arctic sea ice velocity field can be divided into a mean and fluctuating field with the fluctuating field not behaving significantly different from a turbulent fluid (Rampal et al., 2009). It is therefore not sufficient to evaluate models with first order mean velocity fields as these can be predicted correctly by even simple sea ice models (i.e., using a viscous rheology). Second order sea ice deformation fields (strain rates) have to be used for comparison to take into account the high frequency fluctuations of the sea ice velocity field and to assess the quality of the sea ice rheology formulation.

Sea ice strain rates do not scale linearly in space and time but follow a power law depending on the length scale $L$ and time interval $\Delta T$ over which the strain rates are integrated. For RGPS deformation rates $\dot{D}$ in the Arctic, Marsan et al. (2004) and Stern and Lindsay (2009) observe a scale dependence of $\dot{D} \approx dL^{-0.2}$ over a scale range from 10 to 10000 km. The constant $d$ can be interpreted as the mean deformation rate at a given base scale. To make meaningful comparisons between observations and model simulations both have to be brought to the same reference frame in space and time, i.e., averages have to be calculated for the same area and time interval. Otherwise the scaling nonlinearity will cause unphysical differences between the datasets.

It can be shown that traditional sea ice models using the Hibler (1979) viscous-plastic (VP) or elastic-visco-plastic (EVP) (Hunke and Dukowicz, 1997) ice rheology have difficulties in correctly representing the sea ice deformation fields, especially the distribution of the observed linear kinematic features (LKFs) (Kwok et al., 2008; Lindsay et al., 2003; Wang and Wang, 2009). Girard et al. (2009) also report distinct differences in the statistical scaling behavior of RGPS data and models using a VP and EVP sea ice rheology, for example they show that the modeled deformation distributions can be close to Gaussian while the observed ones follow a power law. Some improvement in modeling sea ice deformation and thickness can be obtained by

The Cryosphere Discuss., doi:10.5194/tc-2016-13, 2016
Manuscript under review for journal The Cryosphere
Published: 22 February 2016


modifying the form of the yield curve away from an elliptical shape and/or changing the ratio of major to minor axes (Wang and Wang, 2009; Miller et al., 2005). To overcome some of the deficiencies of the viscous-plastic rheology, new ice rheologies with improved ice physics are under development in the hope of better representing the observed sea ice dynamics (e.g., Heil and Hibler, 2002; Sulsky et al., 2007; Girard et al., 2011; Bouillon and Rampal, 2015b). A recent example is the study of Tsamados et al. (2013), which demonstrates how an anisotropic ice rheology changes the sea ice mass balance and ice dynamics compared to the EVP rheology. Current VP and EVP sea ice model implementations, however, are robust and their parameters well tuned to reproduce the broad features of sea ice extent and drift. Therefore, they are widely used in coupled ocean-sea ice and in global climate simulations and thus their evaluation is necessary.

The main purpose of this article is to examine how model grid spacing influences simulated sea ice deformation representation when compared to satellite observations. In comparison to previous studies we focus on direct comparison between the modeled and observed strain rates. We reconstruct the observed sea ice deformation over the same spatial and temporal scales from the model simulations (section 4.2). In addition we also compare the power law scaling properties of modeled and observed deformation rates (section 4.4). To motivate this study we show in section 3 how the model sea ice strength parameterization and thereby ice deformation influences the sea ice mass balance in the Arctic Ocean. This sensitivity study is similar to the one in Steele et al. (1997) but extends it by also taking changes in sea ice export into account. Itkin et al. (2014) show that the model sea ice strength parametrization as a consequence also can effect the Atlantic Ocean circulation. Ultimately, we would like to raise the attention why improvements in the sea ice strength representation and the ice rheology should receive more attention in models.

The remainder of this article is laid out as follows: Section 3 describes the model and shows how changes in sea ice deformation lead to changes of sea ice volume in the Arctic Basin. This motivates the model to data comparisons in the following sections. Section 4 introduces the RGPS satellite data and contains the comparison between modeled sea ice deformation and RGPS observations. Section 4.3 contains an evaluation of the representation of sea ice deformation dependencies on horizontal grid spacing both spatially and as time series, and section 4.4 shows the power law scaling behavior of the modeled and observed sea ice deformation fields. Finally, Section 5 concludes and further discusses the results.

## 2 MITgcm Arctic Model Setup

The model output used for this study is obtained from integrations of a coupled ocean and sea ice configuration of the Massachusetts Institute of Technology general circulation model (MITgcm) (e.g., Losch et al., 2010). The model configuration is similar to that used for global integrations by the Estimating the Circulation and Climate of the Ocean, Phase II (ECCO2) project (Menemenlis et al., 2008), but only a sub-domain covering the Arctic Ocean including the surrounding marginal seas and parts of the North Atlantic and Pacific is used (see Figure 1).

Briefly, the ECCO2 project uses a cube-sphere grid projection in a volume-conserving C-grid configuration. The ocean model has 50 vertical levels and employs the K-Profile Parameterization (KPP) of Large et al. (1994) for vertical mixing. The cold halocline layer of the Arctic Ocean is realistically reproduced with the use of the subgrid-scale brine rejection parameterization

The Cryosphere Discuss., doi:10.5194/tc-2016-13, 2016
Manuscript under review for journal The Cryosphere
Published: 22 February 2016


of Nguyen et al. (2009). The sea ice model uses 2-category, zero-layer thermodynamics (Hibler, 1980) and viscous-plastic (VP) dynamics (Zhang and Hibler, 1997; Hibler, 1979). The snow cover is simulated following Zhang et al. (1998). Table 1 summarizes the relevant sea ice parameters used for all model solutions presented herein.

The International Bathymetric Chart of the Arctic Ocean (IBCAO) (Jakobsson et al., 2008) is used as bathymetry, where available. For the remaining part of the model domain, which is not covered by IBCAO, the merged Smith and Sandwell/General Bathymetric Charts of the Oceans (GEBCO) is used and blended with IBCAO along the borders. Sea ice initial conditions (area and thickness) for January 1992 are from the Polar Science Center (Zhang and Rothrock, 2003) and ocean initial conditions (temperature, salinity, velocity) are from the World Ocean Atlas 2005 (Locarnini et al., 2006; Antonov et al., 2006). As lateral boundary conditions the globally optimized simulation from ECCO2 (Menemenlis et al., 2008) are used. Surface boundary conditions are obtained from the Japanese 25-year ReAnalysis (JRA-25; Onogi et al., 2007) with a spatial and temporal resolution of $1.125°$ ($\approx 120$ km) and 6 hours, respectively. These spatial and temporal resolutions do not allow to fully resolve all high frequency atmospheric forcing on the sea ice. Some ice deformation events will be missed, which adds uncertainty to the derived sea ice deformation rates by the model.

Integrations with three different nominal horizontal grid spacings, 18 km, 9 km and 4.5 km, were performed. The 18-km model solution was constrained by least squares fit to available satellite and in-situ data using a Green's function approach (Menemenlis et al., 2005) and is here referred to as the "baseline" simulation. A comprehensive evaluation of the 18-km model simulation can be found in Nguyen et al. (2011). They show, by comparison to measurements, that the model using the optimized parameter set can realistically reproduce most important features of the coupled Arctic ocean and sea ice system. For example, sea ice extent and thickness as well as their trends are in good agreement with satellite and in situ measurements. Also the sea ice export through Fram Strait is modeled realistically compared to observations from Kwok et al. (2004). For the higher resolution (9 km and 4.5 km grid spacing) simulations we use the same set of parameters as those derived for the 18-km configuration. As a consequence these higher-resolution simulations exhibit somewhat larger model drifts relative to observations than the 18-km simulation. They nevertheless have been found of sufficient quality for process studies in the Arctic Ocean and adjacent seas (Nguyen et al., 2012; Rignot et al., 2012).

## 3 Sensitivity of Modeled Sea Ice Mass Balance on Ice Strength Parameterization

Changes in ice strength modifies the mechanical redistribution of sea ice through ridging, rafting and open water production, and thus the local ice thickness distribution. Furthermore sea ice strength alters the sea ice drift speed and thereby the sea ice export out of the Arctic Ocean. On a broader scale, changes in sea ice deformation therefore can alter the equilibrium sea ice volume. In this section we perform a set of sensitivity experiments to test the sensitivity of our 18-km model to changes in sea ice deformation to motivate the importance of sea ice deformation for the Arctic sea ice mass balance. Comparisons to satellite data start in section 4.

The sea ice deformation rate

$$\dot{D} = \sqrt{\dot{\nabla}^2 + \dot{\tau}^2} \tag{1}$$

The Cryosphere Discuss., doi:10.5194/tc-2016-13, 2016
Manuscript under review for journal The Cryosphere
Published: 22 February 2016


is used as a measure for the overall sea ice deformation (e.g., Stern and Lindsay, 2009). $\dot{D}$ is the square root of the sum of squares of divergence $\dot{\nabla}$ and shear $\dot{\tau}$. Sea ice deformation is controlled by the strength of the sea ice. In our model configuration the following typical sea ice pressure (strength) $P$ formulation is used (Hibler, 1979):

$$P = P^* h\, e^{[C^*(1-C)]} \tag{2}$$

The ice strength $P$ depends linearly on the ice thickness $h$ and exponentially on the ice concentration $C$. $P^*$ and $C^*$ are scaling constants for the ice strength parameterization. In the optimized Arctic solution with 18-km horizontal grid spacing of Nguyen et al. (2011), $P^* = 23\,\mathrm{kN/m^2}$ and $C^* = -20$ are used. Therefore the value of $P^* = P_0^* = 23\,\mathrm{kN/m^2}$ is used as a baseline and will be compared to two solutions with $P^* = 16\,\mathrm{kN/m^2}$ (70% of baseline value, named "$0.7P_0^*$") and $P^* = 7\,\mathrm{kN/m^2}$ (30% of baseline value, named "$0.3P_0^*$").

The $P^*$ value of $16\,\mathrm{kN/m^2}$ is within the range of values used in current sea ice models (Martin and Gerdes, 2007), while the $P^*$ of $7\,\mathrm{kN/m^2}$ is at the lower end of the used $P^*$ values and can be considered weak ice. We note that the original value of $P^* = 5\,\mathrm{kN/m^2}$ in Hibler (1979), which was even lower than the values we use in this study, is still used and found appropriate for modern setups (e.g., Miller et al., 2005). All model simulations were carried out for the period 1992 to 2009.

The mean sea ice deformation rate $\overline{D}$ and sea ice volume $\overline{V}$ within the Arctic Basin, and export of Arctic sea ice volume $\overline{E}$ are analyzed. Figure 2a shows the borders of the Arctic Basin used here. Export $\overline{E}$ is calculated as the sum of sea ice volume fluxes through all red boundaries. All analyses are based on monthly mean values, including the deformation rate calculation.

Figure 2b shows the seasonal cycle of deformation rates $\overline{D}$ for the 1992–2009 period As expected the deformation rate increases for weaker sea ice. The monthly deformation rate $\overline{D}$ increases by 10% for $0.7P_0^*$ (green) and by 37% for $0.3P_0^*$ (red) compared to the baseline integration (blue). As the deformation rate does not scale linearly, the higher $\overline{D}$ values for $0.3P_0^*$ are expected. All three deformation rates show a clear seasonal cycle with a maximum in August and September and a minimum during February to April. The sea ice speed (not shown) shows a similar behavior with higher ice speeds for weaker ice. Consequences of these sea ice deformation and speed changes on the sea ice mass balance are discussed in the remainder of this section.

### 3.1 Changes in Arctic Basin Sea Ice Volume

In this section, we will discuss the differences in sea ice volume between the three solutions; for a discussion of geophysical sea ice volume change over time, see Nguyen et al. (2011). Figure 3a shows the difference of total sea ice volume $\Delta\overline{V}$ in the Arctic Basin from 1992 to 2009 between the baseline model solution and the $0.7P_0^*$ (green) and $0.3P_0^*$ (red) solutions. The ice volume for the two "weak" solutions starts immediately to diverge from the baseline solution. A similar sensitivity of ice thickness to the choice of the ice strength parameter $P^*$ was reported by Steele et al. (1997) and Itkin et al. (2014).

In 2000, after 8 years, the sea ice volume has increased by 7% and 35% for $0.7P_0^*$ and $0.3P_0^*$, respectively, compared to the baseline. In 2009, at the end of the integration, the differences are 6% ($870\,\mathrm{km^3}$) and 45% ($6700\,\mathrm{km^3}$), respectively. The1992–2009 mean sea ice volume in the Arctic Basin is $17607\,\mathrm{km^3}$ for the baseline integration. The sea ice volume of the $0.3P_0^*$ solution quickly diverges from the baseline. The divergence gets smaller after 1999 but continues until about 2005. Thereafter the difference to the baseline slightly decreases again. The $0.7P_0^*$ solution also diverges until 1999 but by a much smaller rate. Thereafter, the difference stays almost constant with a small negative trend.

### 3.2 Sea Ice Export Out of the Arctic Basin

The changes in Arctic Basin sea ice volume can either be caused by changes in ice production/melting (thermodynamic and dynamic) or by changes of the sea ice volume export out of the Arctic Basin. Similar to sea ice volume, also the yearly mean sea ice export $\overline{E}$ for the "weak" experiments diverges from the baseline and for the $0.3P_0^*$ experiment this difference increases over time (not shown). The monthly mean sea ice volume export during 1992–2009 for the baseline integration is $260\,\mathrm{km}^3$/month. More pronounced, however, is the change in seasonal cycle of the volume export. Figure 3b shows the difference in the seasonal cycle of the sea ice export between the two "weak" experiments and the baseline. The seasonal cycle is enhanced for weaker ice: the sea ice export $\overline{E}$ is larger than the baseline during summer months for both the $0.7P_0^*$ and $0.3P_0^*$ experiments (blue shaded area). During winter $\overline{E}$ is lower than the baseline for both experiments (red shaded area). The much lower ice export during winter for the $0.3P_0^*$ experiment, however, causes a large $17\%$ decrease in overall sea ice export. For the $0.7P_0^*$ experiment the summer increase and winter decrease in $\overline{E}$ nearly balance and result in an overall decrease in $\overline{E}$ by only $1.5\%$.

These above results are one example of the non-linear behavior between (a) ice strength and (b) sea ice volume and export. Intuitively one might expect an increase of ice export for weaker ice since the ice speed increases. The ice area export (not shown), however, is smaller for both "weak" experiments during the complete year. Along the Arctic Basin boundaries the reduction in $P^*$ alone therefore does not favor ice export. The increase in ice thickness will partly compensate for the reduction in $P^*$ in the weak experiments (see Equation 2). However, it also shows the anisotropic behavior in ice strength $P$, which, e.g., can cause ice arching north of the the ice exit gateways or lead to a change of the ice circulation pattern (see also Steele et al., 1997). Parts or a combination of these effects can cause the lower ice export during winter for the "weak" experiments.

During summer the difference in sea ice area export between the "weak" experiments and the baseline is minimal, which suggests that already in the baseline simulation the ice along the basin boundaries was close to a free drift state and a further reduction in $P^*$ has little effect on the drift. Together with the increased ice thickness for the "weak" experiments, however, this leads to an increased ice volume export during summer as shown in Figure 3b.

Overall, the decrease in ice export $\overline{E}$ for both "weak ice" experiments explains most of the sea ice volume increase in the Arctic Basin shown in Section 3.1. The cumulative sea ice export from the beginning of the model integration until month $m$ is defined as:

$$\Sigma\overline{E} = \sum_{t=1}^{m} \overline{E}(t)\,.$$

The difference in $\Sigma\overline{E}$ between the baseline and "weak" experiments at the end of the model integration in 2009 ($m = 216$) is $-790\,\mathrm{km}^3$ for the $0.7P_0^*$ experiment and $-9300\,\mathrm{km}^3$ for the$0.3P_0^*$ experiment. This cumulative reduction in ice export will increase the ice volume in the Arctic Basin for the "weak" experiments as it was found in Section 3.1. For the $0.3P_0^*$ experiment, the decrease in $\Sigma\overline{E}$ is even larger than the increase in Arctic Basin sea ice volume of $6700\,\mathrm{km}^3$ at the end of the integration. For the $0.7P_0^*$ experiment, it accounts for 90% of the $870\,\mathrm{km}^3$ ice volume increase. However, we also have to take changes in sea ice production/melting into account as will be discussed next.

### 3.3 Sea Ice Production and Melt

The net Arctic Basin sea ice production (winter) or melting (summer) $\overline{B}$ is calculated as ice volume changes from one month, $m-1$, to the next month, $m$, after adding the sea ice export during month $m$:

$$\overline{B}(m) = \overline{V}(m) - \overline{V}(m-1) + \overline{E}(m)$$

Figure 3c shows the difference in sea ice production/melting $\Delta\overline{B}$ between the "weak" experiments and the baseline simulation. The difference of the monthly time series has high variability and is very noisy and we therefore apply a 5-year running mean to evaluate the long-term changes. For the first 6 years of the integration, the sea ice production $\overline{B}$ for both "weak" experiments increases compared to the baseline but this increase is much stronger for the $0.3P_0^*$ experiment (red). For both "weak" integrations $\Delta\overline{B}$ stays positive until 2001. For the rest of the model integration period, the mean ice production for the "weak" experiments are lower than the baseline. The mean difference in sea ice production for the complete time series is small (identical for $0.7P_0^*$ and $-5\%$ for $0.3P_0^*$ compared to the baseline).

At the beginning of the integration, when all experiments have the same ice thickness distribution, more thick sea ice can be produced by ice deformation in the "weak" experiments. This causes the ice production $\overline{B}$ to increase compared to the baseline. After the strong increase in ice thickness for the "weak" experiments during the first about 8 years (Figure 3a), sea ice formation by ice deformation gets reduced as well as the thermodynamic growth of sea ice. Therefore the difference in ice production decreases again and even gets negative during the second half of the model integration period (red shaded area in Figure 3c).

At the end of the model run, after 18-years, the cumulative sea ice production

$$\Sigma\overline{B} = \sum_{t=1}^{m} \overline{B}(t)$$

for the $0.3P_0^*$ experiment is 5% ($-2600\,\mathrm{km}^3$) lower than the baseline. This reduction in ice production counteracts the strong increase in ice volume caused by the reduced ice volume export for the $0.3P_0^*$ experiment (Section 3.2). For the $0.7P_0^*$ experiment, $\Sigma\overline{B}$ is about equal to that of the baseline simulation. These differences in $\Sigma\overline{B}$ are small compared to the total differences in Arctic Basin sea ice volume $\overline{V}$ between the three experiments (Figure 3a) and also small compared to the volume differences caused by the reduced sea ice export (Figure 3b). The cumulative differences at the end of the time series together with the mean and maximum differences are summarized in Table 2. The results suggest that the largest part of the difference in sea ice volume $\overline{V}$ in Figure 3a is caused by the changed sea ice export $\overline{E}$, especially for the $0.3P_0^*$ experiment. It also, however, becomes evident that changes in ice deformation can cause large changes in ice production (Figure 3c). In the particular case of the $0.3P_0^*$ experiment, the increase in sea ice production during the first 10 years of simulation is followed by a decrease, which happens to approximately cancel out volume change over the complete 18-year simulation period.

### 3.4 Conclusion of Model Ice Strength Sensitivity

The examples presented in this section highlight the importance of sea ice deformation processes in a coupled ocean-sea ice model. By changing the sea ice strength parameterization and thus the overall sea ice deformation in the Arctic Basin, large changes in the sea ice volume, ice export, and ice production can be observed in the model simulations. These changes can be attributed to enhanced sea ice dynamics, which cause, e.g., a stronger seasonal cycle in sea ice production and ice export. Thus sea ice dynamics, including ice deformation processes, should be adequately represented in a sea ice model if the overall sea ice mass balance is to be simulated realistically. We changed the ice strength parameter $P^*$ within the range used by current model setups. As there is not any true real-world equivalent of $P^*$ the best value for $P^*$ is hard to determine and highly uncertain. This uncertainty could well dominate the uncertainties in thermodynamic parameters, e.g., ice albedo (Steele et al., 1997).

## 4 Modeled Sea Ice Deformation Compared to RGPS Observations

In this section, we compare the simulated sea ice deformation distribution to satellite observations. Big differences between observed and modeled sea ice deformation fields have been reported (see also section 1). Kwok et al. (2008) evaluated four common sea ice models with horizontal grid spacing ranging from 9 to 40 km. None of these models could produce realistic distributions of small-scale deformation features and linear kinematic features (LKFs), although the large-scale sea ice deformation pattern was reproduced correctly by some of the models. The model with the smallest grid spacing (9 km) showed the most confined LKFs. It was speculated that if the model grid spacing would be further decreased, the model could eventually produce more realistic details and have a better representation of LKF distribution. Girard et al. (2009) compared the statistics of VP and EVP simulations with 12-km grid spacing to RGPS data and also reported large differences, as did Wang and Wang (2009) and Lindsay and Stern (2003) for different model setups. We use a slightly different approach and reconstruct the RGPS observations from model velocity fields (section 4.2) and explore how the LKF representation changes when the model resolution increases (section 4.3). We also compare the power law scaling between our model simulations and the RGPS data (section 4.4).

### 4.1 RGPS Satellite Observations

The RADARSAT Geophysical Processor System (RGPS) produces sea ice data products covering the Arctic Ocean derived from Synthetic Aperture Radar (SAR) imagery acquired by the Canadian RADARSAT satellite. Details of the analysis procedures can be found in the papers of Kwok (1998) and Kwok and Cunningham (2002). In this study the “Lagrangian ice motion” dataset, one of the eight RGPS data products, is used as initial dataset. Sea ice deformation, i.e., strain rates, are calculated from this ice motion dataset in a very similar way to the RGPS “Lagrangian ice deformation” product.

The 460-km wide swath ScanSAR Wide B (SWB) mode of RADARSAT (Raney et al., 1991) is selected to provide routine coverage of the Arctic Ocean for the RGPS system. The western Arctic Ocean is covered by RADARSAT images approximately once every three days. At the beginning of the season (winter or summer) an initial Lagrangian grid with 10 km grid

The Cryosphere Discuss., doi:10.5194/tc-2016-13, 2016
Manuscript under review for journal The Cryosphere
Published: 22 February 2016


spacing is set up. The movement and deformation of these grid cells are followed throughout the season. Grid cells are removed if they are advected out of the region of interest. Gaps in the ice motion data sets are due to the lack of backscatter contrast for tracking ice features in the SAR imagery. The actual sea ice tracking is very accurate. Lindsay and Stern (2003) report that the median magnitude of displacement differences between buoy drift (via ARGOS positioning) and RGPS motion estimates is 323 m.

RGPS observations are available since November 1996. In this study we use RGPS data from 20 periods (11 winter and 9 summer) or 97 months between 1996 and 2008 (see Table 3).

### 4.2 Simulating RGPS data Using Model Solutions

As a prerequisite for a meaningful comparison, the Lagrangian RGPS observations and Eulerian model output have to be brought to a common reference frame. We use the RGPS Lagrangian reference frame. This ensures that both RGPS and model sea ice strain rates are calculated for the same area and time interval. This procedure avoids differences between the datasets caused by the non-linearity of the strain rate scaling (power law dependence, see Sections 1, 4.4, and 4.5).

Every RGPS Lagrangian point $k(x_i, t_i)$ has a location, time, and time difference $\Delta t$ until the next observation attached to it. From this $\Delta t = t_{i+1} - t_i$ and the new position $x_{i+1}$ the velocity of point $k$ during the time interval $\Delta t$ can be calculated. We are bilinearly interpolating the Eulerian model velocities to the Lagrangian RGPS positions. The mean RGPS time interval $\Delta t$ is about 3 days, but $\Delta t$ varies from a few hours to about two weeks. We interpolate the mean model sea ice velocity during the individual $\Delta t$'s from the daily model output covering the $\Delta t$ time period.

After this consistent RGPS and model sea ice velocity dataset is established, sea ice strain rates are calculated using Delaunay Triangulation. From the triangle area $A$ and the sea ice velocity components $u$ in $x$ direction and $v$ in $y$ direction at the three triangle corners, the following partial derivatives can be calculated using the Divergence Theorem and the line integral around the triangle boundary:

$$\frac{\partial u}{dx} = \frac{1}{A}\oint u dy, \qquad \frac{\partial u}{dy} = -\frac{1}{A}\oint u dx$$
$$\frac{\partial v}{dx} = \frac{1}{A}\oint v dy, \qquad \frac{\partial v}{dy} = -\frac{1}{A}\oint v dx \tag{3}$$

Using Equations 3 the strain-rates divergence $\dot{\nabla}$, shear $\dot{\tau}$, and vorticity $\dot{\zeta}$ can be calculated:

$$\dot{\nabla} = \frac{\partial u}{dx} + \frac{\partial v}{dy}, \tag{4}$$

$$\dot{\tau} = \sqrt{\left(\frac{\partial u}{dx} - \frac{\partial v}{dy}\right)^2 + \left(\frac{\partial u}{dy} + \frac{\partial v}{dx}\right)^2}, \tag{5}$$

$$\dot{\zeta} = \frac{\partial v}{dx} - \frac{\partial u}{dy}. \tag{6}$$

Erroneous cells, which might, e.g., arise due to errors in the ice tracking or from badly defined triangles from the Delaunay triangulation, are filtered out using the following constrains: (1) The triangle cell area $A$ has to be between 5 and 400 km$^2$. For the statistical comparisons and model to RGPS difference calculations, this condition is further restricted to $25 < A < 100\,\text{km}^2$.

The Cryosphere Discuss., doi:10.5194/tc-2016-13, 2016
Manuscript under review for journal The Cryosphere
Published: 22 February 2016


This condition also assures that the length scale of all observations can be considered to be $\sim 10$ km, which is the initial RGPS grid spacing. This is important as sea ice strain rates are scale-dependent (see Section 1). (2) Triangles are not allowed to be overly distorted, i.e., not to be acute. To achieve this condition all angles have to be larger than $10°$. (3) The time interval $\Delta t$ between two observations must be between 12 hours and 7 days. (4) Cells with a deformation rate $\dot{D}$ (see Equation 1) higher than 1 (or 100%) per day are removed. Only filter (4) creates a different number of observations for the RGPS and model dataset (because $\dot{D}$ can differ between model and RGPS). However, to keep the number of observations equal in both datasets, filtered data points from one dataset are also removed from the other one. We do not use a specific smoother as suggested in Bouillon and Rampal (2015a) to remove artificial noise in the sea ice motion fields. This may lead to an overestimation in the magnitude of the scaling exponent $b$ (Bouillon and Rampal, 2015a) investigated in Sections 4.4 and 4.5. We, however, remove acute triangles susceptible to noise and high deformation rates as described above.

## 4.3 Dependence on Model Grid Spacing

### 4.3.1 Spatial Patterns and LKFs: Divergence, Vorticity, and Shear

Figures 4, 5, and, 6 show the monthly November 1999 divergence, vorticity, and shear fields, respectively, obtained from RGPS data and from the three model solutions with $4.5$, 9, and 18 km grid spacing. For all maps both the Lagrangian RGPS data and the reconstructed Lagrangian model solutions (see Section 4.2) were interpolated on the same polar stereographic grid with $12.5$-km grid spacing. This is a slight oversampling for the 18-km model output but an undersampling for the 9 and $4.5$-km model solutions. This means that all differences visible in the model maps (at least for the 9 and $4.5$-km ones) are due to changed behavior of the model physics and can not be attributed to the different model grid spacing alone.

In general, the large-scale sea ice deformation patterns are reproduced by the model for all three grid spacings. In November 1999 a pattern of high divergence (Figure 4) can be observed in the Beaufort Sea and a more convergent situation north of the Chukchi and East Siberian Sea (see Figures 1 and 4 for locations). This pattern is also present in all three model solutions, but much weaker. In the RGPS observations the pattern is broader and covering most of the seasonal sea ice in that region. The high divergence in the Beaufort Sea is accompanied by negative vorticity (Figure 5), which can be observed in the RGPS data as well as in the three model solutions. Also the positive vorticity pattern north of Ellesmere Island with strong LKFs is reproduced in all three model integrations. The same is true for the positive vorticity pattern in the East Siberian Sea and the negative vorticity north of the Laptev Sea.

The RGPS data show strong sea ice shear almost everywhere in the marginal sea ice zone (Figure 6). This area of high shear is only partly reproduced by all three model solutions. All three model solutions show almost no large-scale shear patterns. In the Beaufort and East Siberian Seas, only small areas of high shear are present. From the three deformation variables divergence, shear, and vorticity the agreement between the large scale RGPS and model shear is worst. The agreement of the vorticity patterns between RGPS and models is best. However, the magnitudes of divergence, shear, and vorticity for all three model solutions are much smaller (less than half, see next section) than the RGPS ones. These statements are true not only for

The Cryosphere Discuss., doi:10.5194/tc-2016-13, 2016
Manuscript under review for journal The Cryosphere
Published: 22 February 2016


the November 1999 example shown here but also for almost all of the other months with available RGPS data (see Table 3) and will be further discussed in Section 4.3.2.

The picture changes when the distribution and frequency of occurrence of LKFs are compared. The model solutions for all three grid spacings do have significantly less LKFs than the RGPS data. This is true for all three deformation variables: divergence, shear and vorticity. Between the three model solutions there are, however, significant differences for the LKF distribution. While, e.g., the sea ice shear for the 18-km model solution in Figure 6 shows very little identifiable LKFs, the number of LKFs slightly increase for the 9-km solution and significantly increase for the $4.5$-km solution. The same can be observed for the divergence and vorticity fields. The $4.5$-km model solution always shows the most LKFs and its deformation distribution is most consistent with RGPS observations. This conclusion holds for all 97 months with available RGPS data that were analyzed and will be further discussed in Section 4.3.3.

The large-scale difference in sea ice deformation between RGPS observations and model solutions is not evenly distributed over the Arctic Basin as can already be seen from Figures 4 to 6. Figure 7 shows the deformation rate difference $\Delta\dot{D} = \dot{D}_{\mathrm{RGPS}} - \dot{D}_{\mathrm{MODEL}}$ for the $4.5$, 9, and 18-km solutions during November 1999. All three difference maps are smoothed with a 150-km kernel to remove small scale differences (e.g., LKFs) and highlight the large-scale difference patterns. The large-scale difference patterns are very similar for all three model grid spacings. The representation of large-scale sea ice deformation in the model therefore does not depend on the model grid spacing; as discussed in the last paragraph, however, the small scale deformation distribution does depend on the model grid spacing.

The main differences in $\Delta\dot{D}$ are confined to the seasonal ice zone (outside the black contour in Figure 7). In general the seasonal sea ice is thinner and more mobile than the older, thicker perennial ice. For the perennial ice, $\Delta\dot{D}$ is much smaller and mainly stays below $0.02\,\mathrm{day}^{-1}$. This discrepancy between seasonal and perennial ice hints to a shortcoming of the sea ice rheology used in the simulations. To first order the main difference between seasonal and perennial sea ice is the ice thickness. The model sea ice strength $P$, as defined in Equation 2, depends linearly on ice thickness $h$. Clearly the linear relationship between $P$ and $h$ is not suitable to realistically model sea ice deformation. This is the typical $P$ formulation for a VP or EVP sea ice rheology with two ice classes. Models with more ice thickness classes often use a $P \propto h^{3/2}$ formulation (Rothrock, 1975; Lipscomb et al., 2007), which can be considered more realistic. In times of a changing Arctic environment, however, where seasonal sea ice is becoming the dominant ice type (Comiso, 2012), the problem of large discrepancies in simulated sea ice deformation of the seasonal ice zone will become more severe.

### 4.3.2 Time Series

For this study RGPS observations for 97 months from 20 RGPS observation periods between November 1996 and May 2008 are used (Table 3). Figure 8 shows (a) the time series of sea ice deformation rate $\dot{D}$ and (b) the seasonal cycle of $\dot{D}$ for all 20 RGPS periods (for visual clarity the period means were preferred to the monthly means due to the high month to month variability). Months September and October are not covered by RGPS data. The time series of $\dot{D}$, $|\dot{\nabla}|$, $|\dot{\tau}|$, and $\dot{\zeta}$ behave very similarly. For simplicity we will therefore concentrate the discussion on the deformation rate $\dot{D}$ (Figure 8) but the statistics for all variables are presented in Table 4.

The Cryosphere Discuss., doi:10.5194/tc-2016-13, 2016
Manuscript under review for journal The Cryosphere
Published: 22 February 2016


The RGPS deformation rate (black) is consistently higher than the one of the 4.5-km (+51%), 9-km (+55%), and 18-km (+57%) simulations. Therefore we conclude that the absolute amount of sea ice deformation in our current sea ice model setup is about 50% too low in comparison to RGPS observations and this underrepresentation of deformation is almost independent of model grid spacing during winter months. During summer months, however, the model performance differs depending on horizontal grid spacing and the 4.5-km simulation shows the smallest difference to RGPS observations. This can be seen in the seasonal cycle in Figure 8b where during December to April the three model solutions are indistinguishable and agree within their standard deviation. Only during summer months (June to August) the 4.5-km solution shows a higher deformation rate than the 9-km solution, which again shows a higher deformation rate than the 18-km solution. The RGPS data show a clean, sinusoidal-like seasonal cycle with a clear minimum in March and maximum in August (likely the real maximum would occur during the unobserved month of September). The three model solutions do not show a sinusoidal behavior. They have a clear maximum during August but no defined minimum. $\dot{D}$ is almost constant during January to May. The 4.5-km solution slightly diverges from this behavior and shows a small but, compared to RGPS data, not very pronounced minimum during March. That is, the 4.5-km solution again shows a better performance than the lower-resolution simulations.

The RGPS and all model deformation time series are highly correlated ($R^2 \approx 0.9$). As is the case for the mean deformation rate, however, the variability of the modeled deformation rate is also much smaller than the observed RGPS variability. The standard deviation $\sigma$ of the monthly $\dot{D}$ time series (not shown) is about 50% smaller for the 18, 9, and 4.5-km solutions ($\sigma = 0.4$ to $0.7 \cdot 10^{-2}$ day$^{-1}$) compared to RGPS data ($\sigma = 1.1 \cdot 10^{-2}$ day$^{-1}$, see Table 4). Again the 4.5-km solution performs best.

#### 4.3.3 Percentage of Area Containing 80% of Sea Ice Deformation

As seen in Section 4.3.2, the absolute amount of sea ice deformation in the model is much too low. Nevertheless, in Section 4.3.1 it was shown that the modeled sea ice deformation distribution gets more similar to the observed one if model grid spacing is decreased. In particular, more and better-confined LKFs appear for smaller grid spacing (e.g., Figure 6). To show this change in the sea ice deformation distribution more quantitatively, the percentage $Q$ of area, which contains 80% of the total sea ice deformation rate is calculated:

$$\dot{D}_1 \geq \dot{D}_2 \ldots \dot{D}_{n-1} \geq \dot{D}_n$$

$$0.8 \sum_{i=1}^{n} \dot{D}_i = \sum_{i=1}^{p} \dot{D}_i$$

$$Q = p/n$$

$\dot{D}_i$ are the individual Lagrangian deformation rate observations sorted by their amount. The number of observations $n$ is identical for all model simulations and the RGPS data. The smaller the percentage $Q$ gets, the more localized the deformation is distributed. As $Q$ is normalized by the total deformation rate of each complete dataset (either RGPS or model solution) this

The Cryosphere Discuss., doi:10.5194/tc-2016-13, 2016
Manuscript under review for journal The Cryosphere
Published: 22 February 2016


measure is independent of the absolute amount of deformation rate. Figure 9 shows (a) the time series of $Q$ for all 20 RGPS periods for the three model solutions and the RGPS data and (b) the seasonal cycle of $Q$ (also see Table 4 for statistics).

As expected the area containing 80% of the total sea ice deformation decreases with decreasing model grid spacing. There is a big difference in $Q$ for the 4.5-km simulation ($\overline{Q} = 27\%$) compared to $Q$ of the 9 and 18-km simulations ($\overline{Q} = 38\%$ and $\overline{Q} = 39\%$, respectively). The mean $\overline{Q} = 27\%$ of the 4.5-km simulation comes close to the $\overline{Q} = 22\%$ of the RGPS observations, which shows that the sea ice deformation distribution got considerably more confined for the 4.5-km simulation compared to the other two lower-resolution simulations. This can also be seen in the examples of Figures 4 to 6, which show a strong increase in the number of LKFs when the grid spacing is reduced from 18 and 9 km to 4.5 km. The strain rate distributions for the 18 and 9-km simulations are much more similar. This is confirmed here by the big improvement of $Q$ for the 4.5-km solution. It is not clear why the change in $Q$ is so big for the 4.5-km solution. Disregarding the big difference in the mean deformation rate, the 4.5-km simulation is able to reproduce the fraction of the total area, in which the strong sea ice deformation events are concentrated. However, the seasonal cycle of $Q$ in Figure 9b is strongly enhanced for all three model solutions compared to RGPS observations. While the $Q$ for RGPS data stays fairly constant between 18% to 19% during winter months (December to May) and only increases by about 9% during summer months, all model solution show a big seasonal cycle with a minimum (May) to maximum (August) difference between 15% to 20%. This can also be seen in the increased standard deviation of the monthly time series of $8\%$ for the model solutions and $5\%$ for the RGPS data.

In summary, sea ice deformation in the model solution with the finest grid spacing of 4.5 km is most confined and localized, as had already been seen in the examples of Section 4.3.1. One has to keep in mind, however, that the absolute model deformation is only about half that of the observations. From the three model solutions, the 4.5-km simulation can be considered most consistent with the RGPS observations.

### 4.4 Power Law Scaling of Deformation Rate

The scaling of sea ice strain rates follows a power law. Some details about the nature of this scaling dependence are, e.g., given in Weiss (2003, 2013). The deformation rate $\dot{D}$ depends on the length scale $L$ over which $\dot{D}$ is determined:

$$\dot{D} \approx dL^b \tag{7}$$

$b$ is the scaling exponent, and $d$ a constant of proportionality, which can be interpreted as mean deformation rate at a given base scale. One would therefore not expect $\dot{D}$ to be the same for model solutions with different grid scaling. In the previous sections we avoided this problem by interpolating the model solutions to the RGPS Lagrangian locations. At least for the model solutions with higher or similar spatial scale as the RGPS data, i.e., the 4.5 and 9-km solutions, this will create comparable datasets. Due to its lower spatial scale, the 18-km solution cannot, in theory, fully recreate the RGPS data, regardless of sea ice rheology formulation.

From field experiments (Stern and Moritz, 2002) and satellite RGPS data (Marsan et al., 2004; Stern and Lindsay, 2009), the scaling exponent $b$ in equation 7 was estimated to be $\approx -0.2$ during winter and $\approx -0.3$ during summer in the Arctic. By analyzing 7 years of RGPS data Stern and Lindsay (2009) find $b$ to have a clear seasonal cycle and to be fairly constant at about

The Cryosphere Discuss., doi:10.5194/tc-2016-13, 2016
Manuscript under review for journal The Cryosphere
Published: 22 February 2016


$-0.2$ during winter (November–April). They also suggest that this scaling exponent can be used to compare measurements and model solutions obtained at different scales. Based on the same sea ice drift dataset Bouillon and Rampal (2015a) find an in magnitude about 50% lower scaling exponent (i.e. $b \approx -0.12$ during winter) for the deformation rate. They attribute the higher scaling exponent in the original RGPS data to artificial noise, which they reduce by a smoother.

In this section, we examine whether sea ice deformation in the three model runs with different horizontal grid spacing follow a similar power law scaling as found in observations, and if the power law in equation 7 with a constant exponent $b$ can be used to compare mean absolute deformation rates of model solutions with different grid spacing.

Figure 10a shows the 1992–2008 time series of the mean sea ice deformation rate $\dot{D}$ in the complete model domain of Figure 1 inset. Different to the previous sections and, e.g., Figure 8, the complete model domain is now considered, not only the areas covered by RGPS data. As expected the deformation rate for the 4.5-km model solution (blue, mean $\dot{D} = 0.123/\text{day}$) is consistently higher than that of the 9-km solution (green, mean $\dot{D} = 0.085/\text{day}$, $-31\%$), which itself is higher than that of the 18-km solution (red, mean $\dot{D} = 0.054/\text{day}$, $-36\%$). The variability from year to year of the mean deformation rate is large, especially during summer. Some years, e.g., 1997–1999, have clearly reduced summer deformation rates in comparison to, e.g., the beginning of the 1990s or 2007 and 2008. The deformation rate during 2008, both during summer and winter, is the highest of the complete time series (Figure 10a).

We assume that the model deformation rate $\dot{D}$ follows the same power-law as given in equation 7 and apply a least-squares fit in log space to equation 7:

$$\log(\dot{D}_i) = \log(d) + b\,\log(L_i) \quad (i = 1 \text{ to } 3)$$

with daily mean deformation rates $\dot{D}_i$ from model solutions with grid spacing $L_i$, i.e., in our case 4.5, 9 and 18 km. For all sea-ice-covered areas in the model domain and for the complete time series, the power law scaling exponent $b$ is estimated to be $-0.54$. Figure 10b shows the deformation rate time series for the three model solutions normalized to a length scale of $L = 10\,\text{km}$, using the estimated scaling exponent $b = -054$. The length scale of 10 km was chosen to be comparable to the RGPS data. Using this scaling, the three time series become much more similar than the original ones in Figure 10a. If looked in detail, however, there remain some quite large differences. For example, the mean $\dot{D}$ of the 9-km simulation is now higher than that of the other two simulations; and the standard deviations of all three simulation are still different (not shown: the standard deviation of the 18-km simulation is $> 0.05/\text{day}$ smaller than that of the 9 and 4.5-km simulations).

These differences imply that a single, constant scaling exponent $b$ is not sufficient to make the strain rates of the three model solutions comparable. $b$ varies seasonally and regionally. Figure 10c and d show, respectively, the dependence of sea ice deformation rate $\dot{D}$ on sea ice concentration $C$ and sea ice thickness $h$ for the three model solutions during the complete 1992 to 2008 time series. In Figure 10c, the deformation rate decreases with increasing sea ice concentration for all three model runs and $\dot{D}$ approaches zero for 100% ice-covered grid cells. Also for increasing ice thickness in Figure 10d the deformation rate decreases but in a more exponential way. For sea ice thickness above 2 m, $\dot{D}$ is near zero. It has to be noted that the ice thicknesses $h$ are the effective ice thicknesses of a complete grid cell, which also can contain open water ($C < 100\%$).

The Cryosphere Discuss., doi:10.5194/tc-2016-13, 2016
Manuscript under review for journal The Cryosphere
Published: 22 February 2016


From Figures 10c and d, it becomes clear that the scale dependence is much stronger for small ice concentrations and thicknesses than for large ones. The scaling exponent $b$ gets more negative for weaker sea ice and approaches zero for very strong sea ice, i.e., thick ice and 100% ice concentration (see Section 3 and Equation 2 for how the ice strength dependencies are incorporated in the model). Note that the scaling exponent $b$ approaches zero for 100% ice concentration or very thick ice (the model solutions converge in Figures 10c and d). This is not expected from theory. Since sea ice is simulated as a viscous-plastic material, even at 100% ice-cover a cell should show power-law scaling behavior. In the model, however, the exponential dependence of sea ice strength on ice concentration inhibits the power-law-scaling property of the ice to emerge in 100% ice-covered grid cells and, in general, no power law scaling behavior can be observed in these cases.

There are additional external factors that influence $b$. For free ice drift, $b$ gets more negative as can be seen by the strong dependence on $C$. Therefore, the surrounding geography, i.e., landmasses, influence the scaling exponent with $b$ values closer to zero in channels and near the coast, where the ice cannot drift freely. The estimated power-law scaling factor $b$ represents the balance between all these factors. That is, sea ice concentration, thickness, and geographic location are important contributors to the estimated scaling exponent.

The above factors also explain why the scaling exponent $b = -0.54$ found here for the three simulations is significantly lower than the $b$ values of $-0.3$ to $-0.2$ found for RGPS data by Stern and Lindsay (2009). In the model, $b$ values between $-0.3$ to $-0.2$ are typical for ice concentrations $\geq 80\%$. These are typical ice concentrations for the RGPS region, which rarely extends to the marginal ice zones with low ice concentrations. If the calculation of the scaling exponent $b$ in the model is restricted to the region covered by RGPS data, a mean $b$ value of $\approx -0.2$ is found, which is comparable to the $b$ values found for RGPS data. This scaling exponent, however, is not applicable to the complete Arctic. For this reason, it is difficult to compare sea ice deformation rates obtained at different spatial scales. For direct comparison, strain rates need to be calculated for identical areas, as was done in Section 4.2. At the very least, for meaningful statistical comparisons, the different scaling behavior for different ice concentrations needs to be considered.

In summary, the three simulations with different horizontal grid spacing, i.e., different resolved spatial scales, follow a similar power law scaling as that estimated using RGPS and buoy observations. We attribute most of the differences between simulated and observed scaling factor $b$ to the different sea ice concentration and thickness ranges of each dataset. The simulated power law scaling strongly depends on ice strength, which itself depends on ice concentration and thickness. For strong sea ice, all model solutions converge to comparably small deformation rates.

### 4.5 Probability Density Function

Another way of looking at the power law scaling behavior of sea ice deformation rate is by comparing probability density functions (PDFs) obtained from model solutions and RGPS data (see Section 4.2 for details). For these comparisons, model output was bin-averaged to the same spatial scale, $L = 12.5$ km, and restricted to the same spatial domains and time periods as the RGPS data. PDFs $p$ for deformation rates $\dot{D}$ from all winter (11 years) and summer (9 years) RGPS periods (see Table 3) were then calculated. Figure 11 shows the PDFs for the three model solutions with 4.5 (blue), 9 (green), and 18 km (red) grid spacing and the RGPS data (black) on a log-log scale.

The Cryosphere Discuss., doi:10.5194/tc-2016-13, 2016
Manuscript under review for journal The Cryosphere
Published: 22 February 2016




Similar to the dependence of deformation rate on spatial scale, the PDFs for observed sea ice strain rates also follow a power law. For example, Girard et al. (2009) report that the PDF of RGPS strain rates during January to March 1997 follows a linear relation in log-log space:

$$p(\dot{D}) \propto \dot{D}^n$$

A linear regression was applied to the PDFs in log-log space for the deformation rate range $0.03$–$0.8\,\mathrm{day}^{-1}$, shown as dashed lines in Figure 11. For very small and large deformation rates outside that range, the RGPS PDFs diverge from the power law relationship. The accuracy of the RGPS observations is about 100 m and noisy at that scale. This noise, which is not removed in this study, can cause artificially higher strain rates (Bouillon and Rampal, 2015a). Low deformation rates therefore could be underrepresented in the RGPS PDF, which potentially could explain the deviation from a straight line for low deformation rates in Figure 11. For very high deformation rates the low number of data points causes artificial variability in the PDFs.

The slope of both the winter and summer RGPS PDF is $n \approx -2$ (winter: $n = -2.06 \pm 0.04$; summer: $n = -2.04 \pm 0.05$). This is consistent with Marsan et al. (2004) and Girard et al. (2009), who report winter RGPS PDF slopes of about $-2.5$ for strain rates at the $\approx$10-km scale. During winter, the slope for the PDFs of all three model solutions is very similar (4.5 km: $n = -1.88 \pm 0.02$; 9 km: $n = -1.83 \pm 0.05$; 18 km: $n = -1.87 \pm 0.03$) and agrees well with the RGPS slope. During summer, the model simulation slopes diverge much more from each other and also from the RGPS data (4.5 km: $n = -1.52 \pm 0.05$; 9 km: $n = -1.81 \pm 0.04$; 18 km: $n = -2.15 \pm 0.08$). Interestingly, the 18-km slope is closest to the RGPS slope during summer months.

During winter, the three model solutions show a close-to-ideal power-law scaling over the shown deformation rate range of $10^{-2}$ to $10^{0}\,\mathrm{day}^{-1}$. During summer, the model solutions diverge from the linear fit for small and large deformation rates. As previously discussed, the magnitude of $\dot{D}$ is significantly lower for the three model solutions, with many more very small deformation rates compared to the RGPS data, as can be seen in Figure 11. This, however, is the range where the RGPS data diverge the most from the power-law scaling relationship.

Overall the PDFs for simulated and observed RGPS deformation rates show good agreement. The observed and simulated power law exponents $n$ agree during during both winter and summer months. We do not observe the strong deviation from power-law scaling reported by **?** for model simulations using the VP and EVP sea ice rheology.

## 5 Summary and Concluding Remarks

A realistic representation of sea ice deformation in models is important for accurate simulation of the sea ice mass balance. Sensitivity experiments show a strong dependence of simulated sea ice volume in the Arctic Basin on the sea ice strength parameterization of the model. A weakening of the simulated sea ice increases the ice deformation rate and drift speed. For the same atmospheric surface boundary conditions, a weakened, more deformable sea ice cover produces a different, in our case increased, Arctic Basin sea ice volume state (Section 3.1). This volume increase is caused by a combination of dynamic and thermodynamic processes. In our sensitivity experiments, a weaker ice cover produces more ice volume due to increased

The Cryosphere Discuss., doi:10.5194/tc-2016-13, 2016
Manuscript under review for journal The Cryosphere
Published: 22 February 2016


deformation and new ice growth in leads. The thickening of the ice, however, increases ice strength and decreases sea ice volume export out of the Arctic Basin compared to the baseline experiment (Section 3.2). Thermodynamic growth is also reduced for thicker ice. The balance of these processes leads to a new equilibrium Arctic Basin ice volume after about eight years of simulation.

Multiple equilibrium flow states (ice growth equals ice export) can exist for the Arctic Basin, and their characteristics are influenced by sea ice strength and ice rheology (Hibler et al., 2006). For the last decade of simulation, all sensitivity experiments show a decrease in ice volume, which is consistent with the observed sea ice volume loss (Kwok and Rothrock, 2009; Nguyen et al., 2011). The changing Arctic sea ice volume in the simulations is caused both by changes in sea ice export (Section 3.2) as well as in sea ice production and melting (Section 3.3). The reduced sea ice export, however, makes up the largest part of the volume change. Furthermore, the ocean also shows sensitivity to the amount of sea ice deformation. For the model realizations with weaker ice, i.e., more deformation and ice movement, the ocean mixed layer depth increases during winter time. These model sensitivity experiments therefore illustrate the importance of properly representing sea ice deformation in sea ice models in order to accurately simulate the overall sea ice mass balance.

Arctic ocean and sea ice simulations with horizontal grid spacing of 18, 9, and $4.5$ km were compared to RGPS satellite observations during the 1992–2008 period. Lagrangian sea ice drift was reconstructed from the three model solutions for a direct comparison with the RGPS data. Sea ice strain rate divergence, vorticity, and shear were calculated in the same way for the three simulations and for satellite observations from the Lagrangian ice drift datasets. Even though the viscous-plastic dynamic sea ice model with elliptical yield curve is able to produce what appears to be linear kinematic features (LKFs), the orientation and spatial density of these LKFs are very different from what is observed in the RGPS data. The mean sea ice deformation rate is between 51% to 57% lower in the simulations than in the RGPS data. The largest difference occurs for the magnitude of divergence, which is 67% to 79% too low (Table 4). Also the large-scale shear pattern is not well reproduced in the model solutions (Figure 6). In addition the LKFs occur less frequently in the simulations. Of the three model solutions, the one with the smallest grid spacing of $4.5$ km has characteristics closest to RGPS observations.

While RGPS sea ice deformation data show a clear discrimination between the thinner seasonal sea ice with more deformation and the thicker perennial sea ice, the model deformation zones are mainly confined to a few LKFs at the ice margins. Differences are largest for seasonal sea ice, where the model strongly underestimates sea ice deformation. This suggests a shortcoming of the ice rheology, for example, the linear dependence between ice strength and ice thickness. Model solutions with smaller grid spacing, however, result in more small-scale deformation features. In particular, the 4.5-km simulation has more LKF-like features in the Central Arctic than the coarser-resolution simulations and, visually, the spatial distribution of these LKF-like features agrees better with RGPS observations. This improved realism is evaluated by computing the percentage $Q$ of sea ice area containing 80% of sea ice deformation, which is a measure of how confined the deformation processes are. For this metric, the $4.5$-km model solution performs very similarly to the RGPS data, with a $Q$ value of 27% compared to $Q = 22\%$ for RGPS, while the 9 and 18-km simulations have $Q$ values around 38%. These differences in small-scale deformation features can be important because ocean-to-atmosphere heat transfer tends to occurs on small scales. For example,

The Cryosphere Discuss., doi:10.5194/tc-2016-13, 2016
Manuscript under review for journal The Cryosphere
Published: 22 February 2016


the heat flux from narrow leads can be twice as high as that from larger leads (Marcq and Weiss, 2012) and ocean upwelling events caused by sea ice shear motion happen on small scales (McPhee et al., 2005).

The scaling of the deformation rate in the three model solutions with different grid spacing, i.e., different length scales follows a similar power law as is observed for the RGPS observations (Section 4.4). The power law exponent $b$ for the complete model domain is $-0.54$. If the domain is restricted to the area covered by RGPS observations, consisting of compact, thick ice, the exponent becomes with $b = -0.2$ very similar to what is observed for the RGPS data. The power law scaling exponent therefore strongly depends on ice concentration and thickness, i.e., the internal ice stress. During winter also the probability density functions (PDF) of the three VP model deformation rates are similar to the RGPS data and exhibit the same power law exponent $n \approx -2$. During summer the PDFs of the three model solutions get more different but, however, still follow a power law. We do not observe the strong divergence from power law scaling for the VP sea ice rheology reported by Girard et al. (2009).

On larger scales the sea ice deformation rate of all three model solutions is very similar, with only small improvements for the $4.5$-km simulation (Figure 7). Almost independent of grid spacing, the modeled sea ice deformation is much lower than the RGPS observations ($\sim 50\%$). Bouillon and Rampal (2015a) suggest that RGPS deformation rates are too high due to artificial noise in the motion fields, which could explain part of this difference. Nevertheless, the large scale pattern of divergence(Figure 4) and vorticity (Figure 5), but not shear (Figure 6), are reproduced by all model simulations. Even if the differences are small for the large scale deformation patterns, the $4.5$-km simulation, the one with the smallest horizontal grid spacing, always performs best out of the three solutions. This difference becomes more pronounced if small scale deformation features are considered. The $4.5$-km simulation is the only one that reproduces a reasonable number of LKFs in the Central Arctic, even on length scales ($2\times$ the grid spacing) where the lower resolution models theoretically are capable of reproducing these features. We conclude that increasing the spatial model resolution can improve the sea ice deformation representation for a viscous-plastic sea ice rheology. However, big differences to the observed sea ice deformation strain rates still remain.

An interesting future study would be to attempt to adjust sea ice and ocean model parameters in order to reproduce the metrics discussed in this paper. For example, in a separate sensitivity experiment, not discussed in this manuscript, we changed the sea ice strength dependence on sea ice thickness (Equation 2) from linear to cubic, which considerably increased deformation rate in both perennial and seasonal ice zones. Of course, adjusting a single parameter can improve a certain set of model features but is likely to make others, e.g., sea ice velocity, worse. What is needed is the simultaneous adjustment of several key model parameters, in the manner discussed in Menemenlis et al. (2005) and Nguyen et al. (2011). Other possible approaches for improving the representation of sea ice strain rates include the introduction of multiple categories for different ice thicknesses and deformed and undeformed ice, since multicategory models allow weaker resistance, more leads, and enhanced ice growth (Mårtensson et al., 2012); and experimentation with new ice rheologies that do not rely on the viscous-plastic assumptions (Sulsky et al., 2007; Girard et al., 2011; Tsamados et al., 2013; Bouillon and Rampal, 2015b).

*Acknowledgements.* The constant development and support for the MITgcm from the people involved with mitgcm.org is acknowledged. We thank Martin Losch and Pierre Rampal for constructive discussions about the model and sea ice deformation analysis. This work was performed at the Jet Propulsion Laboratory, California Institute of Technology under contract with the National Aeronautics and Space Administration (NASA). Parts of this research has been supported by the Institutional Strategy of the University of Bremen, funded by the German Excellence Initiative. High End Computing resources were provided by the NASA Advanced Supercomputing Division.

The Cryosphere Discuss., doi:10.5194/tc-2016-13, 2016
Manuscript under review for journal The Cryosphere
Published: 22 February 2016


## References


Antonov, J. I., Locarnini, R. A., Boyer, T. P., Mishonov, A. V., and Garcia, H. E.: World Ocean Atlas 2005, Volume 2: Salinity, vol. 2, NOAA Atlas NESDIS 62, U.S. Government Printing Office, Washington, D.C., S. Levitus, edn., 2006.

Barry, R. G., Serreze, M. C., Maslanik, J. A., and Preller, R. H.: The Arctic Sea Ice-Climate System: Observations and modeling, Rev. Geophys., 31, 397–422, doi:10.1029/93RG01998, 1993.

Bouillon, S. and Rampal, P.: On producing sea ice deformation data sets from SAR-derived sea ice motion, The Cryosphere, 9, 663–673, doi:10.5194/tc-9-663-2015, http://www.the-cryosphere.net/9/663/2015/, 2015a.

Bouillon, S. and Rampal, P.: Presentation of the dynamical core of neXtSIM, a new sea ice model, Ocean Model., 91, 23–37, doi:10.1016/j.ocemod.2015.04.005, http://www.sciencedirect.com/science/article/pii/S1463500315000694, 2015b.

Comiso, J. C.: Large Decadal Decline of the Arctic Multiyear Ice Cover, J. Climate, 25, 1176–1193, doi:10.1175/JCLI-D-11-00113.1, 2012.

Comiso, J. C., Parkinson, C. L., Gersten, R., and Stock, L.: Accelerated decline in the Arctic sea ice cover, Geophys. Res. Lett., 35, L01703, doi:10.1029/2007GL031972, 2008.

Coon, M., Kwok, R., Levy, G., Pruis, M., Schreyer, H., and Sulsky, D.: Arctic Ice Dynamics Joint Experiment (AIDJEX) assumptions revisited and found inadequate, J. Geophys. Res., 112, C11S90, doi:10.1029/2005JC003393, 2007.

Fenty, I., Menemenlis, D., and Zhang, H.: Global coupled sea ice-ocean state estimation, Clim. Dyn., pp. 1–26, doi:10.1007/s00382-015-2796-6, 2015.

Girard, L., Weiss, J., Molines, J. M., Barnier, B., and Bouillon, S.: Evaluation of high-resolution sea ice models on the basis of statistical and scaling properties of Arctic sea ice drift and deformation, J. Geophys. Res., 114, C08015, doi:10.1029/2008JC005182, 2009.

Girard, L., Bouillon, S., Weiss, J., Amitrano, D., Fichefet, T., and Legat, V.: A new modelling framework for sea ice mechanics based on elasto-brittle rheology, Ann. Glaciol., 52, 123–132, 2011.

Heil, P. and Hibler, W. D.: Modeling the High-Frequency Component of Arctic Sea Ice Drift and Deformation, J. Phys. Oceanogr., 32, 3039–3057, doi:10.1175/1520-0485(2002)032<3039:MTHFCO>2.0.CO;2, 2002.

Hibler, W.D., I., Hutchings, J., and Ip, C.: Sea-ice arching and multiple flow states of Arctic pack ice, Ann. Glaciol., 44, 339–344, 2006.

Hibler, W.: A Dynamic Thermodynamic Sea Ice Model, J. Phys. Oceanogr., 9, 815–846, doi:10.1175/1520-0485(1979)009<0815:ADTSIM>2.0.CO;2, 1979.

Hibler, W.: Modeling a Variable Thickness Sea Ice Cover, Mon. Wea. Rev., 108, 1943–1973, doi:10.1175/1520-0493(1980)108<1943:MAVTSI>2.0.CO;2, 1980.

Hunke, E. and Dukowicz, J.: An elastic-viscous-plastic model for sea ice dynamics, J. Phys. Oceanogr., 27, 1849–1867, 1997.

Itkin, P., Karcher, M., and Gerdes, R.: Is weaker Arctic sea ice changing the Atlantic water circulation?, J. Geophys. Res. Oceans, 119, 5992–6009, doi:10.1002/2013JC009633, 2014.

Jakobsson, M., Macnab, R., Mayer, L., Anderson, R., Edwards, M., Hatzky, J., Schenke, H. W., and Johnson, P.: An improved bathymetric portrayal of the Arctic Ocean: Implications for ocean modeling and geological, geophysical and oceanographic analyses, Geophys. Res. Lett., 35, L07602, doi:10.1029/2008GL033520, 2008.

Kwok, R.: The RADARSAT Geophysical Processor System, in: Analysis of SAR Data of the Polar Oceans: Recent Advances, edited by Tsatsoulis, C. and Kwok, R., pp. 235–257, Springer-Verlag, New York, 1998.

Kwok, R. and Cunningham, G. F.: Seasonal ice area and volume production of the Arctic Ocean: November 1996 through April 1997, J. Geophys. Res., 107, 8038, doi:10.1029/2000JC000469, 2002.

The Cryosphere Discuss., doi:10.5194/tc-2016-13, 2016
Manuscript under review for journal The Cryosphere
Published: 22 February 2016


Kwok, R. and Rothrock, D. A.: Decline in Arctic sea ice thickness from submarine and ICESat records: 1958–2008, Geophys. Res. Lett., 36, L15501, doi:10.1029/2009GL039035, 2009.

Kwok, R., Cunningham, G. F., and Pang, S. S.: Fram Strait sea ice outflow, J. Geophys. Res., 109, C01009, doi:10.1029/2003JC001785, 2004.

Kwok, R., Hunke, E. C., Maslowski, W., Menemenlis, D., and Zhang, J.: Variability of sea ice simulations assessed with RGPS kinematics, J. Geophys. Res., 113, C11 012, doi:10.1029/2008JC004783, 2008.

Large, W., McWilliams, J., and Doney, S.: Oceanic vertical mixing: a review and a model with a nonlocal boundary layer parameterization, Rev. Geophys., 32, 363–403, 1994.

Lindsay, R. W. and Stern, H. L.: The RADARSAT Geophysical Processor System: Quality of Sea Ice Trajectory and Deformation Estimates, J. Atmos. Oceanic Technol., 20, 1333–1347, doi:10.1175/1520-0426(2003)020<1333:TRGPSQ>2.0.CO;2, 2003.

Lindsay, R. W., Zhang, J., and Rothrock, D. A.: Sea-Ice Deformation Rates from Satellite Measurements and in a Model, Atmos. Ocean, 41, 35–47, doi:10.3137/ao.410103, 2003.

Lindsay, R. W., Zhang, J., Schweiger, A. J., Steele, M. A., and Stern, H.: Arctic sea ice retreat in 2007 follows thinning trend, J. Climate, 22, 165–176, doi:10.1175/2008JCLI2521, 2009.

Lipscomb, W. H., Hunke, E. C., Maslowski, W., and Jakacki, J.: Ridging, strength, and stability in high-resolution sea ice models, J. Geophys. Res., 112, C03S91, doi:10.1029/2005JC003355, 2007.

Locarnini, R. A., Mishonov, A. V., Antonov, J. I., Boyer, T. P., and Garcia, H. E.: World Ocean Atlas 2005, Volume 1: Temperature, vol. 1, NOAA Atlas NESDIS 61, U.S. Government Printing Office, Washington, D.C., S. Levitus, edn., 2006.

Losch, M., Menemenlis, D., Campin, J.-M., Heimbach, P., and Hill, C.: On the formulation of sea-ice models. Part 1: Effects of different solver implementations and parameterizations, Ocean Modelling, 33, 129–144, doi:10.1016/j.ocemod.2009.12.008, http://www.sciencedirect.com/science/article/pii/S1463500309002418, 2010.

Marcq, S. and Weiss, J.: Influence of sea ice lead-width distribution on turbulent heat transfer between the ocean and the atmosphere, The Cryosphere, 6, 143–156, doi:10.5194/tc-6-143-2012, http://www.the-cryosphere.net/6/143/2012/, 2012.

Marsan, D., Stern, H., Lindsay, R., and Weiss, J.: Scale dependence and localization of the deformation of Arctic sea ice, Phys. Rev. Lett., 93, 178501, doi:10.1103/PhysRevLett.93.178501, 2004.

Mårtensson, S., Meier, H. E. M., Pemberton, P., and Haapala, J.: Ridged sea ice characteristics in the Arctic from a coupled multicategory sea ice model, J. Geophys. Res., 117, C00D15, doi:10.1029/2010JC006936, 2012.

Martin, T. and Gerdes, R.: Sea ice drift variability in Arctic Ocean Model Intercomparison Project models and observations, J. Geophys. Res., 112, C04S10, doi:10.1029/2006JC003617, 2007.

McPhee, M. G., Kwok, R., Robins, R., and Coon, M.: Upwelling of Arctic pycnocline associated with shear motion of sea ice, Geophys. Res. Lett., 32, L10616, doi:10.1029/2004GL021819, 2005.

Menemenlis, D., Fukumori, I., and Lee, T.: Using Green's Functions to Calibrate an Ocean General Circulation Model, Mon. Wea. Rev., 133, 1224–1240, doi:10.1175/MWR2912.1, 2005.

Menemenlis, D., Campin, J., Heimbach, P., Hill, C., Lee, T., Nguyen, A., Schodlock, M., and Zhang, H.: ECCO2: High Resolution Global Ocean and Sea Ice Data Synthesis, Mercator Ocean Quarterly Newsletter, 31, 13–21, 2008.

Miller, P. A., Laxon, S. W., and Feltham, D. L.: Improving the spatial distribution of modeled Arctic sea ice thickness, Geophys. Res. Lett., 32, L18503, doi:10.1029/2005GL023622, 2005.

Nghiem, S. V., Rigor, I. G., Perovich, D. K., Clemente-Colón, P., Weatherly, J. W., and Neumann, G.: Rapid reduction of Arctic perennial sea ice, Geophys. Res. Lett., 34, L19504, doi:10.1029/2007GL031138, 2007.

Nguyen, A. T., Menemenlis, D., and Kwok, R.: Improved modeling of the Arctic halocline with a subgrid-scale brine rejection parameterization, J. Geophys. Res., 114, C11014, doi:10.1029/2008JC005121, 2009.

Nguyen, A. T., Menemenlis, D., and Kwok, R.: Arctic ice-ocean simulation with optimized model parameters: Approach and assessment, J. Geophys. Res., 116, C04025, doi:10.1029/2010JC006573, 2011.

Nguyen, A. T., Kwok, R., and Menemenlis, D.: Source and Pathway of the Western Arctic Upper Halocline in a Data-Constrained Coupled Ocean and Sea Ice Model, J. Phys. Oceanogr., 42, 802–823, doi:10.1175/JPO-D-11-040.1, 2012.

Onogi, K., Tsutsui, J., Koide, H., Sakamoto, M., Kobayashi, S., Hatsushika, H., Matsumoto, T., Yamazaki, N., Kamahori, H., Takahashi, K., Kadokura, S., Wada, K., Kato, K., Oyama, R., Ose, T., Mannoji, N., and Taira, R.: The JRA-25 Reanalysis, J. Meteor. Soc. Japan, 85, 369–432, 2007.

Rampal, P., Weiss, J., Marsan, D., and Bourgoin, M.: Arctic sea ice velocity field: General circulation and turbulent-like fluctuations, J. Geophys. Res., 114, C10014, doi:10.1029/2008JC005227, 2009.

Raney, R., Luscombe, A., Langham, E., and Ahmed, S.: RADARSAT [SAR imaging], Proceedings of the IEEE, 79, 839–849, doi:10.1109/5.90162, 1991.

Rignot, E., Fenty, I., Menemenlis, D., and Xu, Y.: Spreading of warm ocean waters around Greenland as a possible cause for glacier acceleration, Ann. Glaciol., 53, 257–266, doi:10.3189/2012AoG60A136, http://www.ingentaconnect.com/content/igsoc/agl/2012/00000053/00000060/art00032, 2012.

Rothrock, D. A.: The Energetics of the Plastic Deformation of Pack Ice by Ridging, J. Geophys. Res., 80, 4514–4519, 1975.

Steele, M., Zhang, J., Rothrock, D., and Stern, H.: The force balance of sea ice in a numerical model of the Arctic Ocean, J. Geophys. Res., 102, 21 061–21 079, doi:10.1029/97JC01454, 1997.

Stern, H. L. and Lindsay, R. W.: Spatial scaling of Arctic sea ice deformation, J. Geophys. Res., 114, C10017, doi:10.1029/2009JC005380, 2009.

Stern, H. L. and Moritz, R. E.: Sea ice kinematics and surface properties from RADARSAT synthetic aperture radar during the SHEBA drift, J. Geophys. Res., 107, 8028, doi:10.1029/2000JC000472, 2002.

Sulsky, D., Schreyer, H., Peterson, K., Kwok, R., and Coon, M.: Using the material-point method to model sea ice dynamics, J. Geophys. Res., 112, C02S90, doi:10.1029/2005JC003329, 2007.

Tsamados, M., Feltham, D. L., and Wilchinsky, A. V.: Impact of a new anisotropic rheology on simulations of Arctic sea ice, J. Geophys. Res. Oceans, 118, 91–107, doi:10.1029/2012JC007990, 2013.

Wang, K. and Wang, C.: Modeling linear kinematic features in pack ice, J. Geophys. Res., 114, C12011, doi:10.1029/2008JC005217, 2009.

Weiss, J.: Scaling of fracture and faulting of ice on Earth, Surv. Geophys., 24, 185–227, 2003.

Weiss, J.: Drift, Deformation, and Fracture of Sea Ice – A Perspective Across Scales, SpringerBriefs in Earth Sciences, Springer Netherlands, doi:10.1007/978-94-007-6202-2, 2013.

Zhang, J. and Hibler, W. D., I.: On an efficient numerical method for modeling sea ice dynamics, J. Geophys. Res., 102, 8691–8702, doi:10.1029/96JC03744, 1997.

Zhang, J. and Rothrock, D. A.: Modeling Global Sea Ice with a Thickness and Enthalpy Distribution Model in Generalized Curvilinear Coordinates, Mon. Wea. Rev., 131, 845–861, doi:10.1175/1520-0493(2003)131<0845:MGSIWA>2.0.CO;2, 2003.

The Cryosphere Discuss., doi:10.5194/tc-2016-13, 2016
Manuscript under review for journal The Cryosphere
Published: 22 February 2016


Zhang, J., Hibler, W. D., Steele, M., and Rothrock, D. A.: Arctic ice-ocean modeling with and without climate restoring, J. Phys. Oceanogr., 28, 191–217, 1998.

Zhang, J., Thomas, D. R., Rothrock, D. A., Lindsay, R. W., Yu, Y., and Kwok, R.: Assimilation of ice motion observations and comparisons with submarine ice thickness data, J. Geophys. Res., 108, 3170, doi:10.1029/2001JC001041, 2003.

Zhang, J., Lindsay, R., Steele, M., and Schweiger, A.: What drove the dramatic retreat of arctic sea ice during summer 2007?, Geophys. Res. Lett., 35, L11505, doi:10.1029/2008GL034005, 2008.

The Cryosphere Discuss., doi:10.5194/tc-2016-13, 2016
Manuscript under review for journal The Cryosphere
Published: 22 February 2016


**Figures**

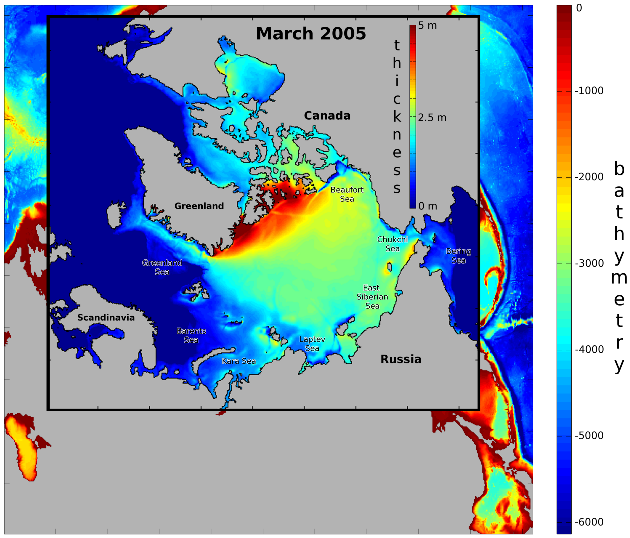


**Figure 1.** The Arctic face of the cube sphere grid used by the ECCO2 project. The March 2005 ice thickness inset shows the regional grid used in this study. Note that North Pacific coastline in regional grid is modified relative to global set-up in order to remove unconnected seas. Boundary conditions are obtained from the ECCO2 18-km cube sphere solution.

The Cryosphere Discuss., doi:10.5194/tc-2016-13, 2016
Manuscript under review for journal The Cryosphere
Published: 22 February 2016


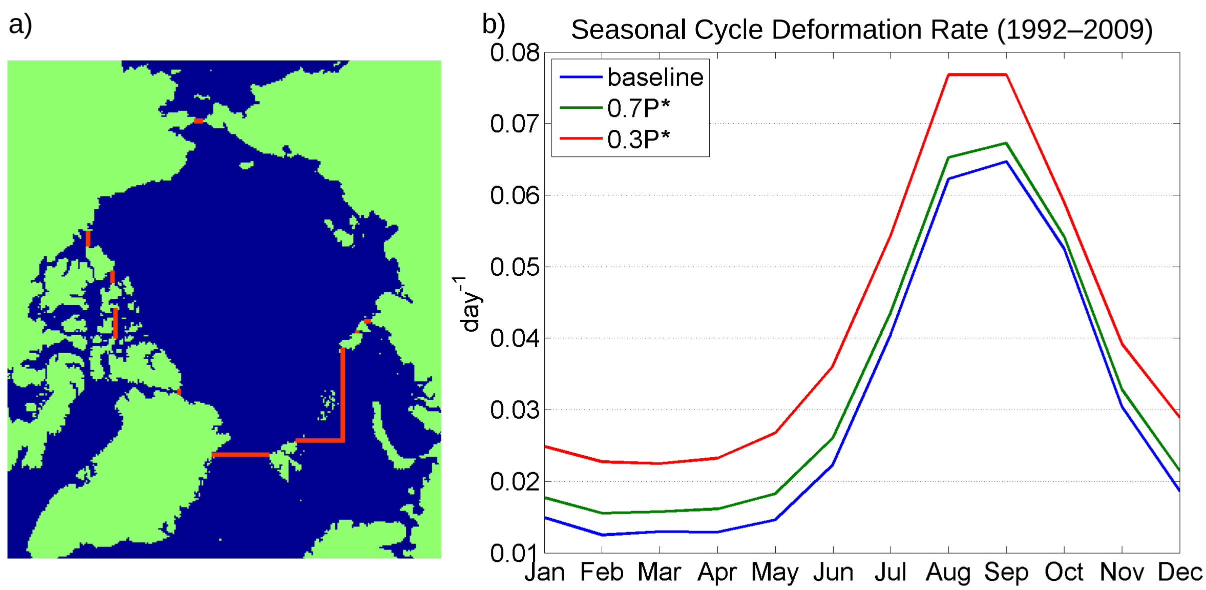


**Figure 2.** a) Red lines mark the Arctic Basin boundaries and flux gates used. b) Seasonal cycle (1992–2009) of mean monthly deformation rate $\overline{D}$ within the Arctic Basin for the three experiments baseline in blue, $0.7P_0^*$ in green, and $0.3P_0^*$ in red.

The Cryosphere Discuss., doi:10.5194/tc-2016-13, 2016
Manuscript under review for journal The Cryosphere
Published: 22 February 2016


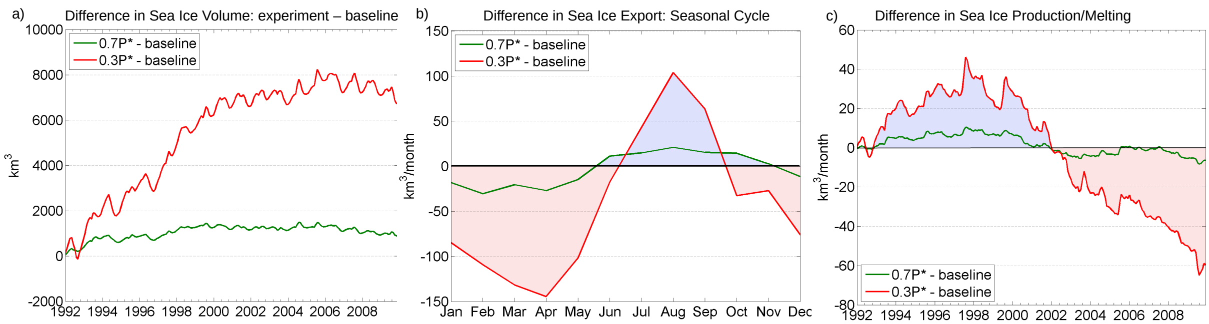


**Figure 3.** Differences between simulations for "$0.7P_0^*$ − baseline" in green and "$0.3P_0^*$ − baseline" in red. a) Difference in Arctic Basin sea ice volume, b) difference in seasonal cycle of sea ice export, and c) difference in sea ice production/melting (5-year running mean).

The Cryosphere Discuss., doi:10.5194/tc-2016-13, 2016
Manuscript under review for journal The Cryosphere
Published: 22 February 2016


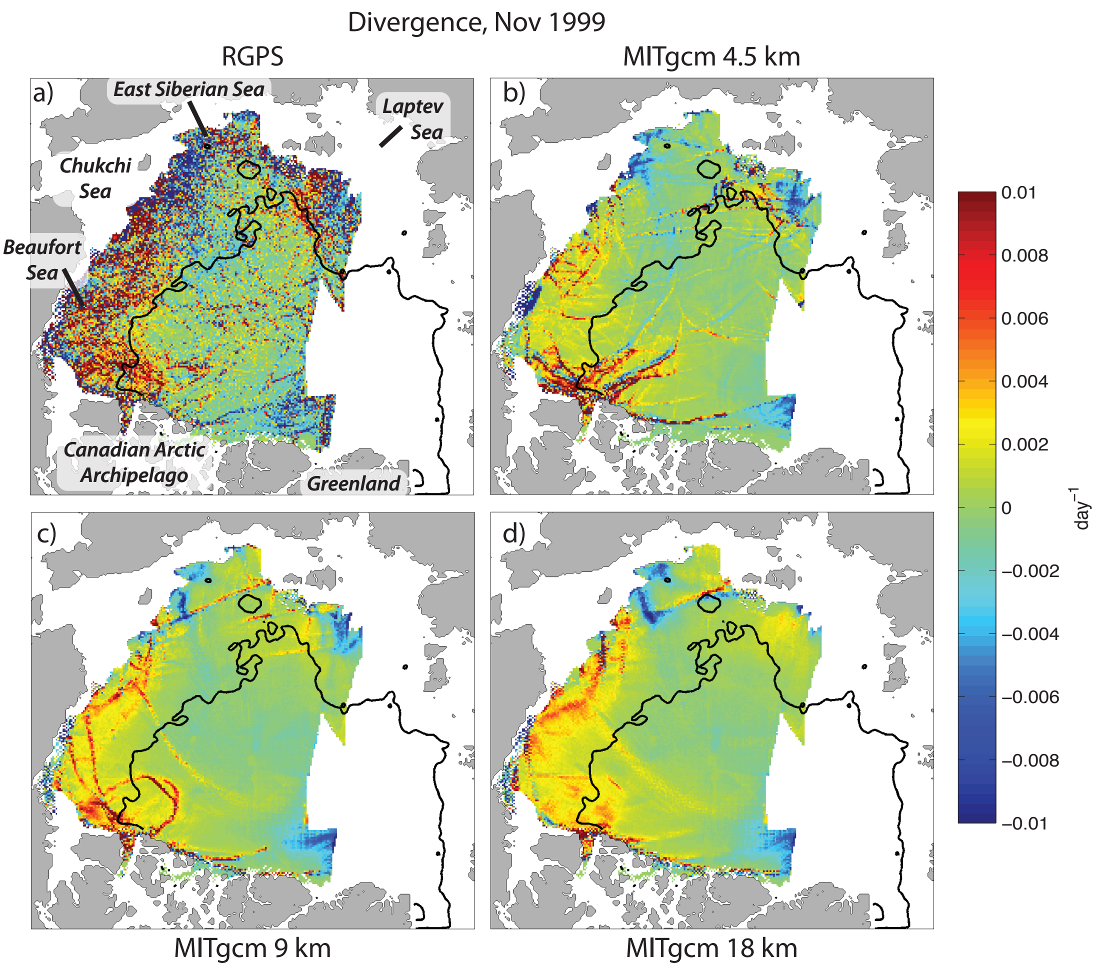


**Figure 4.** Examples of monthly mean November 1999 sea ice divergence. The divergence from (a) RGPS and the model runs with (b) 4.5-km, (c) 9-km, and (d) 18-km grid spacing are shown. The number of LKFs increases with decreasing model grid spacing. All maps are shown on the same 12.5 km grid and are constructed from the same number of observations (see Section 4.2). The black line discriminates seasonal and perennial sea ice. White areas are not covered by RGPS observations.

The Cryosphere Discuss., doi:10.5194/tc-2016-13, 2016
Manuscript under review for journal The Cryosphere
Published: 22 February 2016


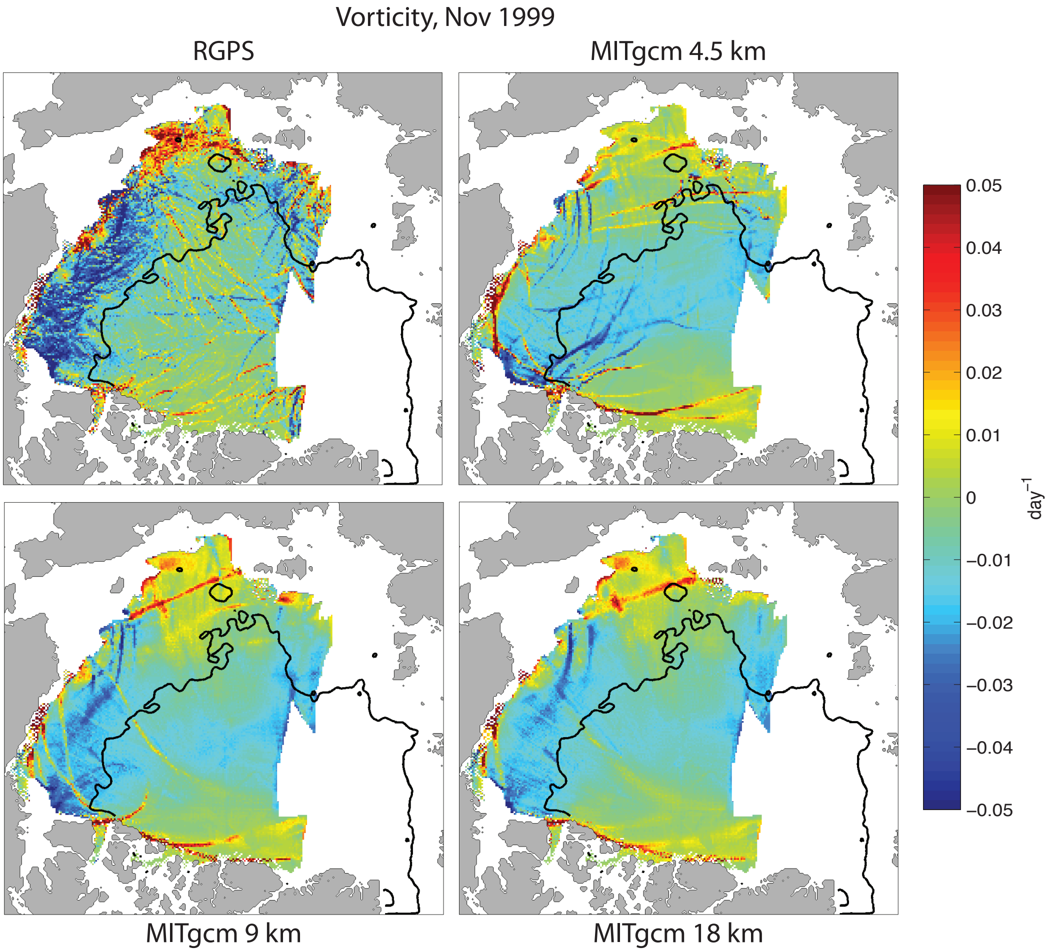


**Figure 5.** As Figure 4 but for vorticity.

The Cryosphere Discuss., doi:10.5194/tc-2016-13, 2016
Manuscript under review for journal The Cryosphere
Published: 22 February 2016


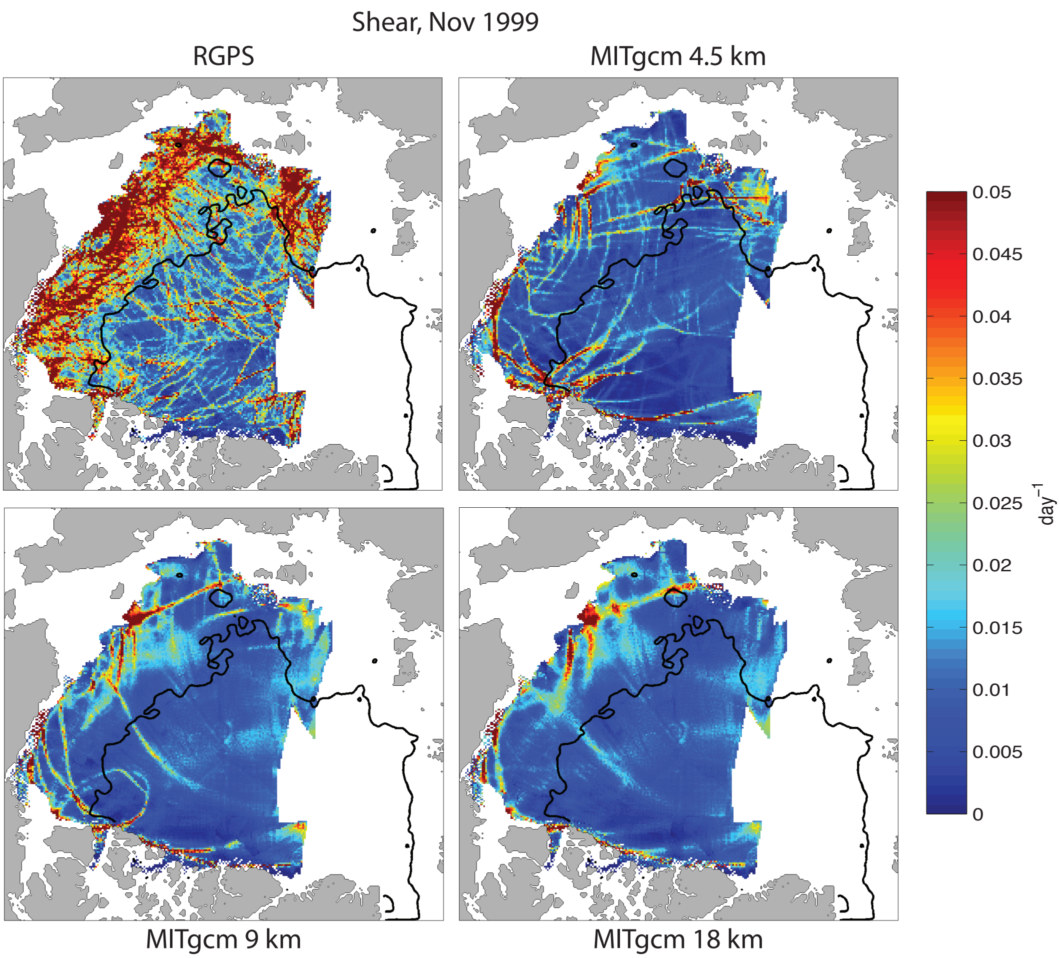


**Figure 6.** As Figure 4 but for shear.

The Cryosphere Discuss., doi:10.5194/tc-2016-13, 2016
Manuscript under review for journal The Cryosphere
Published: 22 February 2016


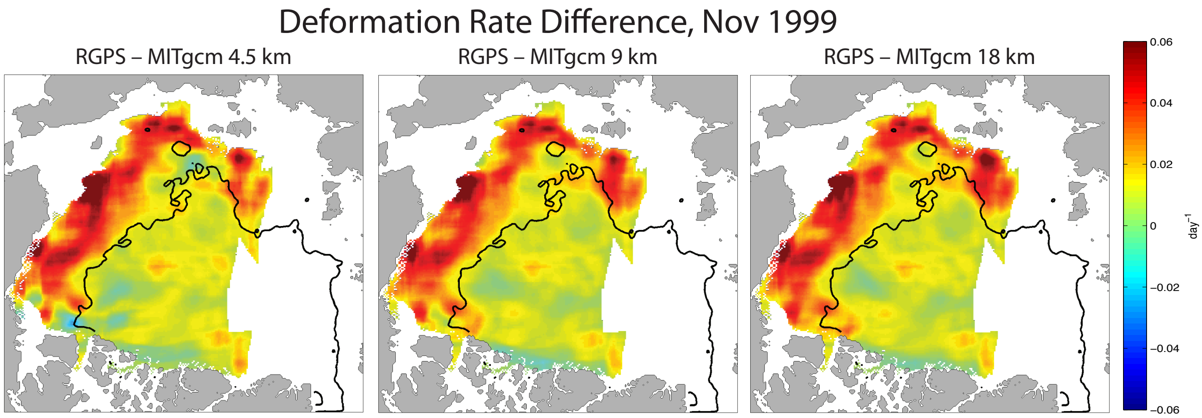


**Figure 7.** Smoothed (150 km) difference in deformation rate $\dot{D}$ between RGPS and model solutions with 4.5 km (left), 9 km (middle), and 18 km (right) grid spacing. Largest differences occur in the seasonal ice zone outside the black contour.

The Cryosphere Discuss., doi:10.5194/tc-2016-13, 2016
Manuscript under review for journal The Cryosphere
Published: 22 February 2016




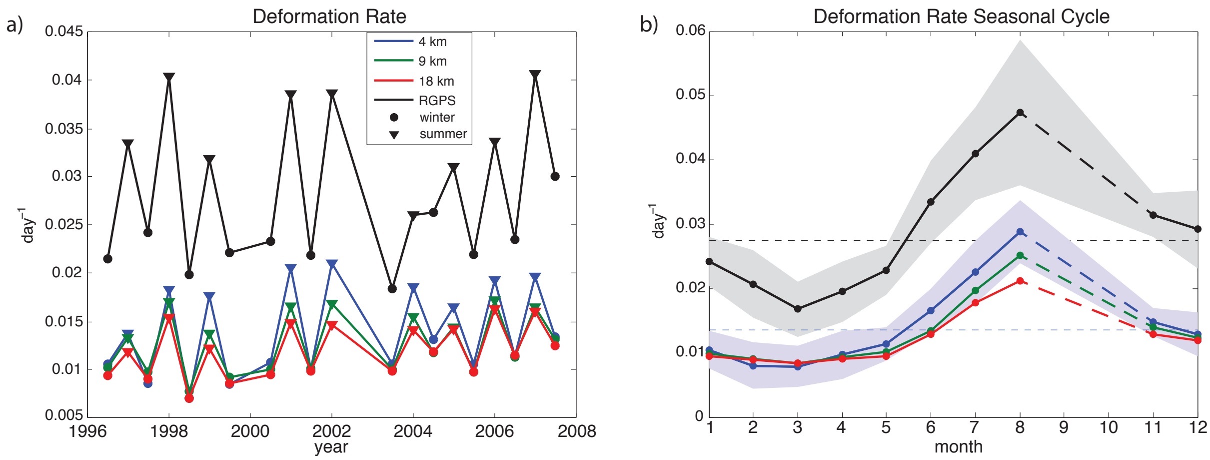


**Figure 8.** a) Mean deformation rate $\dot{D}$ for all 20 RGPS periods and the corresponden modeled values. Circles mark winter periods and triangles summer periods; note that periods have different length (see Table 3). b) Seasonal cycle of $\dot{D}$; shaded areas show standard deviations for RGPS and the 4.5-km solution (9 and 18-km solutions are similar); dashed lines show the mean calculated from the monthly time series; note that no data is available for September and October.

The Cryosphere Discuss., doi:10.5194/tc-2016-13, 2016
Manuscript under review for journal The Cryosphere
Published: 22 February 2016


The Cryosphere Discussions
Open Access

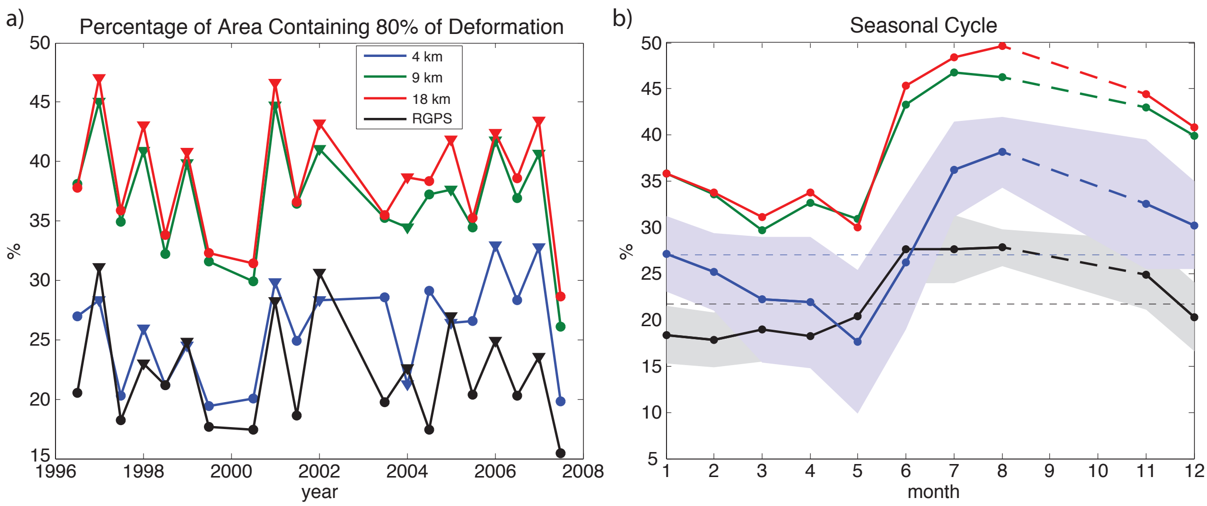


**Figure 9.** Percentage $Q$ of area containing 80% of the overall sea ice deformation rate. a) time series showing the absolute percentage for RGPS data (black) and model solutions with 4.5 (blue), 9 (green), and 18 km (red) grid spacing for all 20 RGPS periods. Circles mark winter periods and triangles summer periods; note that periods have different length (see Table 3). b) Seasonal cycle of $Q$; shaded areas show standard deviations for RGPS and the 4.5-km solution (9 and 18-km solutions are similar); dashed lines show the mean calculated from the monthly time series; note that no data is available for September and October.

The Cryosphere Discuss., doi:10.5194/tc-2016-13, 2016
Manuscript under review for journal The Cryosphere
Published: 22 February 2016


The Cryosphere
Discussions
Open Access

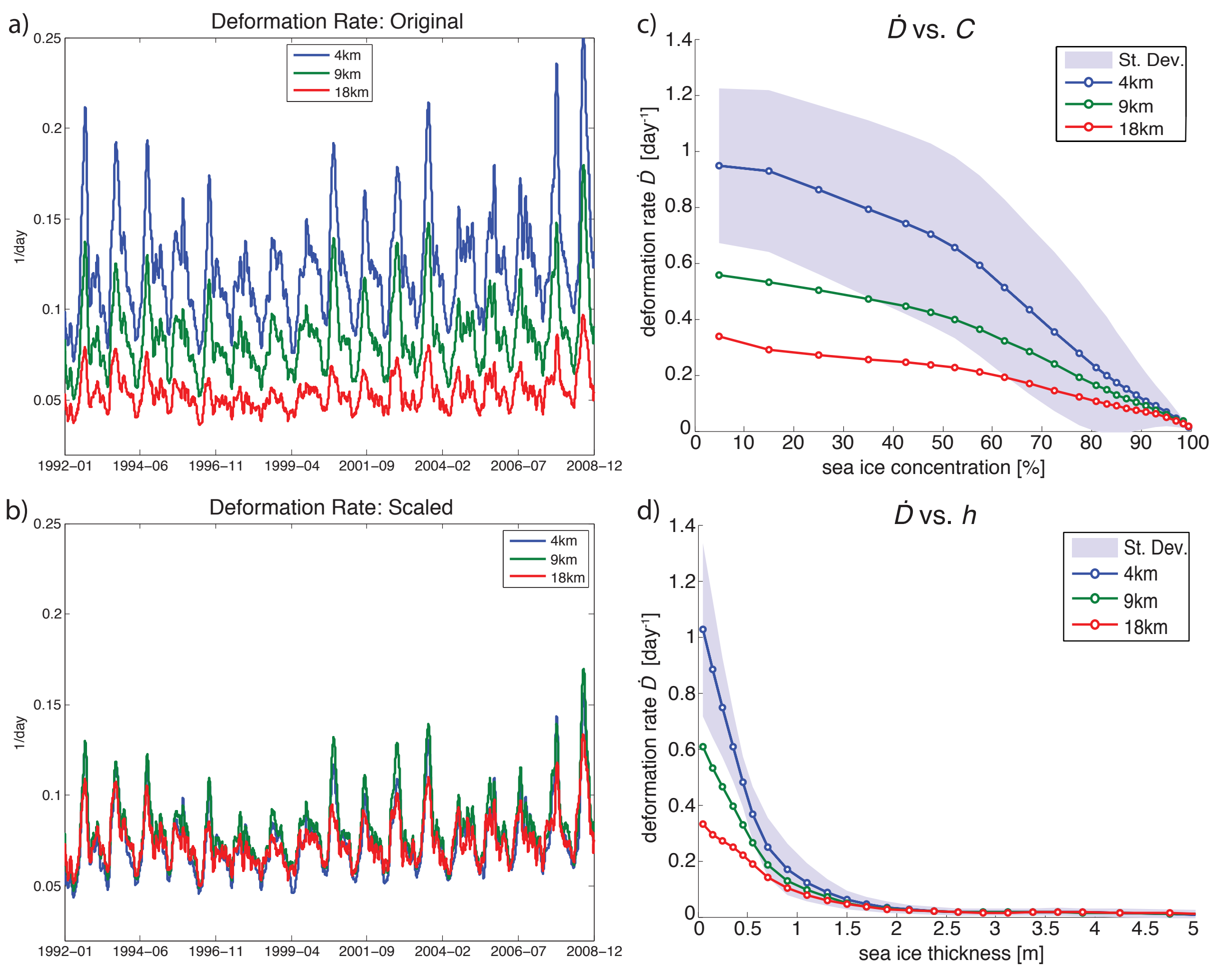


**Figure 10.** a) Time series 1992–2008 of mean deformation rate $\dot{D}$ in the complete model domain (see Fig. 1) for model runs with 4.5 (blue), 9 (green), and 18 km (red) grid spacing. b) as a) but for deformations normalized to a 10 km scale using equation 7 with $b = -0.54$. All curves are one month running means. c) and d) show, respectively, the dependence of sea ice deformation rate $\dot{D}$ on sea ice concentration $C$ and sea ice thickness $h$ for the three model integrations. Blue shaded color areas mark ± one standard deviation for the 4.5 km solution (9 and 18-km solutions are similar).

The Cryosphere Discuss., doi:10.5194/tc-2016-13, 2016
Manuscript under review for journal The Cryosphere
Published: 22 February 2016


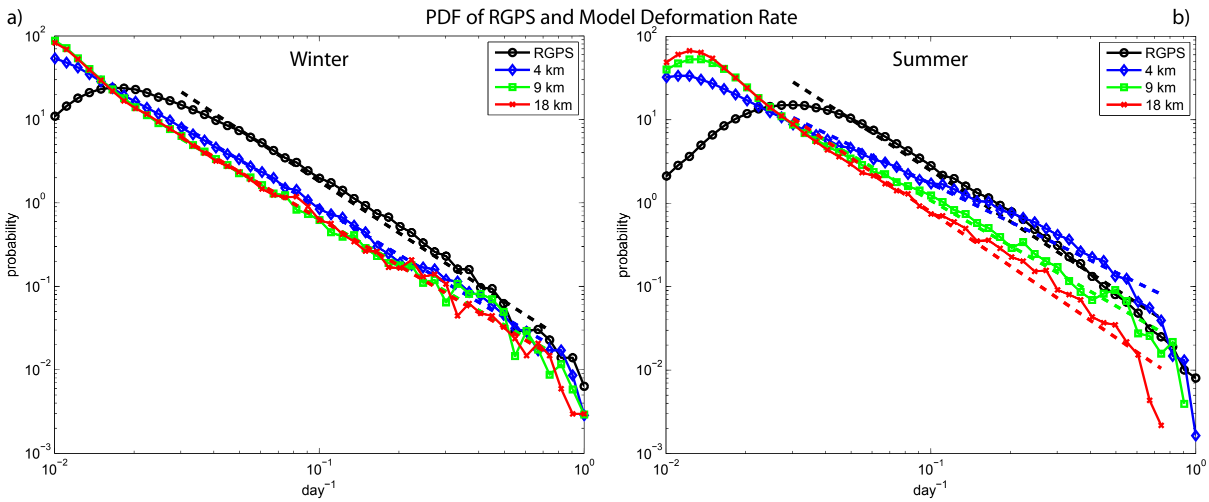


**Figure 11.** Probability density function of sea ice deformation rate $\dot{D}$ for all a) winter (Nov–Apr) and b) summer (May–Jun) periods for RGPS and model solutions. Dashed lines are least square fits to the approximately linear part of the PDFs between 0.03 and 0.8 $\mathrm{day}^{-1}$. Note the logarithmic axes scaling.

The Cryosphere Discuss., doi:10.5194/tc-2016-13, 2016
Manuscript under review for journal The Cryosphere
Published: 22 February 2016


## Tables

**Table 1.** Selected sea ice model parameters

| | | |
|---|---|---|
| Atmospheric forcing | JRA-25 | |
| Sea ice dry albedo | 0.7 | |
| Sea ice wet albedo | 0.71 | |
| Snow dry albedo | 0.87 | |
| Snow wet albedo | 0.81 | |
| Ocean albedo | 0.16 | |
| Air/sea ice drag coefficient | 0.0011 | |
| Ocean/sea ice drag coefficient | 0.0054 | |
| Ice strength parameter $P^*$ | 23 | kN/m$^2$ |
| Lead closing parameter $H_o$ | 0.6 | |
| elliptical yield curve major to minor axis ratio $e$ | 2 | |

The Cryosphere Discuss., doi:10.5194/tc-2016-13, 2016
Manuscript under review for journal The Cryosphere
Published: 22 February 2016


**Table 2.** Difference in Arctic Basin sea ice volume $\Delta\overline{V}$, cumulative ice export $\Delta\Sigma\overline{E}$, and cumulative sea ice production $\Delta\Sigma\overline{B}$ between the two experiments and the baseline.

| | End (Dec 2009) | | Mean | | Max. | |
|---|---|---|---|---|---|---|
| in km$^3$ | $0.7P_0^*$ | $0.3P_0^*$ | $0.7P_0^*$ | $0.3P_0^*$ | $0.7P_0^*$ | $0.3P_0^*$ |
| $\Delta\overline{V}$ | 870 | 6700 | 1050 | 5480 | 1490 | 8230 |
| $\Delta\Sigma\overline{E}$ | -790 | -9300 | -660 | -4340 | -940 | -9460 |
| $\Delta\Sigma\overline{B}$ | 80 | -2600 | 390 | 1140 | 810 | 3130 |

**Table 3.** RGPS periods used in this study. Column 3 gives the number of monthly mean values used.

| start date | end date | no. months | season |
|---|---|---|---|
| 1996-11-07 | 1997-06-01 | 7 | winter |
| 1997-05-18 | 1997-08-01 | 2 | summer |
| 1997-11-02 | 1998-06-01 | 7 | winter |
| 1998-05-10 | 1998-09-01 | 2 | summer |
| 1998-10-28 | 1999-05-17 | 6 | winter |
| 1999-05-08 | 1999-09-01 | 4 | summer |
| 1999-11-01 | 2000-05-14 | 7 | winter |
| 2000-11-04 | 2001-06-01 | 7 | winter |
| 2001-05-15 | 2001-09-01 | 3 | summer |
| 2001-11-05 | 2002-06-01 | 7 | winter |
| 2002-05-16 | 2002-08-01 | 2 | summer |
| 2003-12-04 | 2004-06-01 | 6 | winter |
| 2004-05-11 | 2004-09-01 | 3 | summer |
| 2004-11-10 | 2005-06-01 | 7 | winter |
| 2005-05-15 | 2005-09-01 | 3 | summer |
| 2005-11-29 | 2006-06-01 | 6 | winter |
| 2006-05-19 | 2006-09-01 | 3 | summer |
| 2006-12-03 | 2007-06-01 | 6 | winter |
| 2007-05-14 | 2007-09-01 | 3 | summer |
| 2007-12-01 | 2008-06-01 | 6 | winter |
| 20 periods (11 winter/9 summer) | | 97 | |

The Cryosphere Discuss., doi:10.5194/tc-2016-13, 2016
Manuscript under review for journal The Cryosphere
Published: 22 February 2016


**Table 4.** Overview of some statistical parameters for the complete 97-month time series of RGPS and model sea ice strain rates. All units are $10^{-2}$ day$^{-1}$ if not otherwise indicated; $\pm$ values denote the standard deviation of the time series; 'difference' is the difference between model and RGPS in %; and 'correlation' is the correlation coefficient between the model and RGPS time series.

| $\cdot 10^{-2}$ | | RGPS | 4.5 km | 9 km | 18 km |
|---|---|---|---|---|---|
| deformation rate $\dot{D}$ | mean | $2.8 \pm 1.1$ | $1.4 \pm 0.7$ | $1.3 \pm 0.5$ | $1.2 \pm 0.4$ |
| | difference | | $-51\%$ | $-55\%$ | $-57\%$ |
| | correlation | | 0.89 | 0.90 | 0.90 |
| magnitude of divergence $\lvert\dot{\nabla}\rvert$ | mean | $1.1 \pm 0.5$ | $0.4 \pm 0.2$ | $0.3 \pm 0.2$ | $0.2 \pm 0.1$ |
| | difference | | $-67\%$ | $-77\%$ | $-79\%$ |
| | correlation | | 0.85 | 0.87 | 0.86 |
| magnitude of vorticity $\lvert\dot{\tau}\rvert$ | mean | $2.3 \pm 0.7$ | $1.4 \pm 0.6$ | $1.3 \pm 0.4$ | $1.2 \pm 0.4$ |
| | difference | | $-40\%$ | $-43\%$ | $-47\%$ |
| | correlation | | 0.82 | 0.84 | 0.82 |
| shear $\dot{\zeta}$ | mean | $2.4 \pm 0.9$ | $1.3 \pm 0.6$ | $1.2 \pm 0.5$ | $1.1 \pm 0.4$ |
| | difference | | $-47\%$ | $-50\%$ | $-53\%$ |
| | correlation | | 0.89 | 0.90 | 0.90 |
| percentage of area containing 80% of deformation $Q$ | mean | $22 \pm 5\%$ | $27 \pm 8\%$ | $38 \pm 8\%$ | $39 \pm 8\%$ |
| | difference | | 24% | 72% | 78% |
| | correlation | | 0.49 | 0.72 | 0.77 |